Object-oriented modelling of a tracked vehicle for agricultural applications

Computers and Electronics in Agriculture 230 (2025) 109921

Contents lists available at ScienceDirect

Computers and Electronics in Agriculture

journal homepage: www.elsevier.com/locate/compag

Original papers

Object-oriented modelling of a tracked vehicle for agricultural applications

Alessandro Febbraro [a], Mattia Dutto [a,b], Luca Bascetta [a], Gianni Ferretti [a,*]

[a] Politecnico di Milano, Department of Electronics, Information and Bioengineering, Piazza Leonardo da Vinci, 32, 20133 Milano, Italy
[b] Politecnico di Torino, Department of Control and Computer Engineering, Corso Duca degli Abruzzi, 24, 10129 Torino, Italy

ARTICLE INFO

Dataset link: https://github.com/ROSETEA-lab/modelica_agilexbunker

Keywords:
Agricultural robotics
Tracked vehicle
Modelling
Simulation
Modelica language

ABSTRACT

Mobile robots are a pillar of technologies that support agriculture 4.0, tracked mobile robots in particular are very suitable for agricultural applications. In this paper, the development of the multibody model of a tracked vehicle for agricultural applications is described, with the main goal to create a tool for the design of motion planning and control strategies in realistic conditions, in particular taking into account the characteristics of the terrain (terramechanics). Thanks to the modular approach enabled by the object-oriented modelling language Modelica, the complete suspension system as well as the interaction of tracks and grousers with the terrain have been described with a high level of accuracy. An extensive campaign of validation experiments has been carried out, mainly focused on the steering dynamics: on a rigid surface in indoor experiments and on a deformable surface in outdoor experiments. In indoor experiments the actual position of robot center of mass and its angular orientation were measured very accurately through a VICON motion capture system and an Inertial Measurement Unit (IMU), in outdoor experiments the motion capture system was replaced by a Real-Time Kinematic (RTK) Global Positioning System (GPS). This validation campaign has demonstrated the accuracy of the proposed model in representing the vehicle dynamics, clearly stating that it can be profitably adopted as a tool to design and validate novel planning and control strategies for agricultural robots.

1. Introduction

Over the last decade, agriculture has undergone a transformation known as Agriculture 4.0 (Liu et al., 2021). This revolution is driven by various factors, including climate change, population growth, land degradation, increasing resource scarcity, labour shortages, economic recession, and de-globalization, with a primary focus on minimizing agriculture's environmental impact.

Agriculture 4.0 is built upon two key components: precision agriculture and smart farming, both of which harness modern information and communication technologies. Precision agriculture, as defined by Pierce and Nowak (1999), involves "the application of farming strategies and methodologies to do the right thing, in the right place, at the right time", thereby optimizing resource use – such as water, agrochemicals, arable land, and fertilizers – while maintaining yield and minimizing environmental harm. Smart farming (Gebbers and Adamchuk, 2010) employs sensing technologies, software applications, communication systems, positioning tools, hardware, and data analytics to enhance both the quantity and quality of agricultural products while optimizing labour requirements.

Among the various technologies under the umbrella of smart farming, mobile robots and autonomous vehicles play a pivotal role (Bascetta and Ferretti, 2024; Goel et al., 2021; Subeesh and Mehta, 2021; Marinoudi et al., 2019). These innovations significantly boost production efficiency without compromising environmental sustainability (Said Mohamed et al., 2021). In addition to improving environmental outcomes, these technologies also enhance working conditions for farmers, reducing the risk of musculoskeletal disorders associated with physically demanding tasks (Fathallah, 2010; Proto and Zimbalatti, 2010; Zhang et al., 2019b). Furthermore, they contribute to increased profitability, product quality, and crop yields, particularly when applied to tasks such as crop monitoring, harvesting, and pruning (Zhang et al., 2019c).

Extensive reviews (Botta et al., 2022; Yépez-Ponce et al., 2023; Tiozzo Fasiolo et al., 2023; Droukas et al., 2023) highlight the diverse applications of mobile robots and autonomous vehicles across various agricultural tasks, including weed control, seeding, fertilizing, pest management, crop harvesting, sowing, planting, pruning, thinning, and disease monitoring (Slaughter et al., 2008; Bechar and Vigneault, 2017; Zhang et al., 2019a).

Among the different types of available robots, tracked mobile platforms are very suitable for agricultural applications (Elaoud and Chehaibi, 2011; Kutzbach, 2000), and can be classified into two main categories: vehicles with rigid or flexible tracks. In the

* Correspondence to: Politecnico di Milano, Cremona Campus, Via Sesto, 39, 26100 Cremona, Italy.
E-mail address: gianni.ferretti@polimi.it (G. Ferretti).

https://doi.org/10.1016/j.compag.2025.109921
Received 18 September 2024; Received in revised form 21 November 2024; Accepted 4 January 2025
Available online 14 January 2025

first category the track belts structure consists of a solid chain track made of steel plates, whereas in the second category the track belts are made of rubber reinforced with steel wires along the longitudinal length. A common aspect of the two types of tracks is the capability to deform upon contact with the soil and adapt to it to some extent, and this makes the dynamic modelling of a tracked robot more complex with respect to the wheeled one, in particular, the description of the interaction with the terrain calls for a distributed model of the track belt (Ferretti and Girelli, 1999).

In order to design planning and motion control strategies, an accurate model of the tracked robot is needed. In the literature several approaches are reported, where the simplest one focuses on kinematics only, while the most accurate approach for the description of the dynamics of a tracked robot is based on multibody models. In turn, multibody models of tracked robots can be mainly classified based on the adopted multibody environment:

- MSC ADAMS® (Automated Dynamic Analysis of Mechanical Systems) (Mocera and Nicolini, 2018; Nicolini et al., 2018; Mocera et al., 2020; Grazioso et al., 2022b, 2023);
- Simulink® (Özdemir, 2016; Özdemir et al., 2016, 2017; Grazioso et al., 2022a; Miller, 2024);
- object-oriented modelling environments (Ferretti and Girelli, 1999), and the model developed in this work.

Another important classification of multibody models can be based on the model of the terrain, either rigid (Özdemir, 2016; Özdemir et al., 2016, 2017; Mocera and Nicolini, 2018; Grazioso et al., 2022b, 2023; Miller, 2024) or deformable (Ferretti and Girelli, 1999; Nicolini et al., 2018; Mocera et al., 2020; Grazioso et al., 2022a).

One of the most accurate multibody model of a tracked vehicle developed in the MSC ADAMS® environment is the one created by Mocera and Nicolini (2018). This study concerns the modelling of a small size farming tracked vehicle with rigid tracks and moving on hard ground, as a preliminary step for a future Hardware-In-the-Loop simulation of a full vehicle on a mechatronic real time test bench (Bosso et al., 2013; Mocera and Soma, 2017). In this study the rigid tracks are modelled as a series of 40 rigid links connected together with low friction rotational joints. The model's behaviour was then compared with the kinematic behaviour considering three different scenarios: a forward motion on a horizontal terrain, a mixed case where the vehicle approached a slope of 20 degrees after a horizontal start, and a pivot turn, to investigate the lateral behaviour; no experimental data were collected.

Another study performed in the MSC ADAMS® environment is the one of Nicolini et al. (2018). This paper is mainly focused on the modelling of the interaction between the tracks of the farming tracked vehicle considered in Mocera and Nicolini (2018) and a deformable soil, also in this case the model was developed for a future design of control strategies. Simulations considered first a rigid ground and the same three different scenarios considered in Mocera and Nicolini (2018), then the case of a deformable terrain was considered, focusing in particular on the pressure distribution under the tracks, the track sinkage, the trend of the vertical force acting on different links when the vehicle approaches an obstacle on sand, and the traction force-slip curves; also in this case no field experiments were performed.

Another study of Mocera et al. (2020), using the same farming tracked vehicle considered in Mocera and Nicolini (2018) and Nicolini et al. (2018), investigates the effect of the presence of the grousers on the traction force-slip curves, assuming a deformable terrain. A track model without grousers was first considered, taking into account a rigid ground and the same three different scenarios selected in Mocera and Nicolini (2018), then a deformable terrain was introduced to study the normal pressure distribution, the track sinkage and the traction force-slip curves. Finally, the complete model of the tracked vehicle with the grousers moving over a soft sandy terrain and over a compact terrain was simulated, in this case the sinkage for different grouser heights and the traction force-slip curves was analysed. As expected, in the case of a soft sandy terrain, the maximum traction force developed by a track with grousers was greater than the one developed by smooth tracks, while in the case of compact agricultural soil the maximum value of the traction force was smaller than the value reached with smooth grousers, this is due to the fact that soil stiffness does not allow the grousers to sink completely; no experiment was anyway performed.

Other two studies based on the MSC ADAMS® environment are the ones of Grazioso et al. (2022b, 2023). In this case a multibody model of an agricultural tracked robot with flexible (rubber) tracks was developed, modelling each rubber track through the finite volume approach, by dividing it into 56 discrete segments. In both papers the virtual multibody model, once validated, is used to evaluate the performance of the suspension system. Experimental tests and simulations have been performed on hard terrain only.

The Matlab/Simulink® environment was adopted in the works of Özdemir (2016) and Özdemir et al. (2016, 2017), mainly focused on the development of a general transient steering model and of a general transient contact and slip model for tracked vehicles on flat and hard ground. The modelled vehicle has rigid tracks, and each contact area of the track links is divided in four cells. The experiments performed in field tests were a circular steering with a step input, a double lane change, and a pivot turn. The comparison between field tests and simulations for circular steering with step input and double lane change manoeuvrers showed a very good agreement of the trajectories, while for pivot turn the error for a complete turn was 9.8%, the yaw rate of the tested vehicle was slower than the one obtained in simulation.

In the paper of Grazioso et al. (2022a) a multibody model of a track, still developed in the Matlab/Simscape® environment, is used to evaluate the pressure distribution upon contact with a deformable terrain. More precisely, the vehicle considered in this paper consists of a rear-wheel axle and a wheel/track reconfigurable front axle, which can adjust the contact area with the ground. The model was mainly developed to quantify the pressure distribution along the contact area and to use this quantification to design the contact area based on the soil conditions to minimize soil damage, while considering the rolling resistance and traction performance.

The Matlab/Simscape® environment is also adopted in a very recent work concerning the multibody modelling of a tracked vehicle (Miller, 2024), where a package containing two multibody models has been developed: a model of an excavator tracks and a model of an articulated tracked vehicle, in both cases the vehicles are moving on an uneven rigid soil.

The work of Ferretti and Girelli (1999) is focused on the modelling of an agricultural tracked vehicle moving on a deformable terrain, with the main goals of motion analysis and control system design. A partial differential equation (PDE) describing the variation of the shear displacement with respect to longitudinal position on track and time is derived, and, under the assumption of linear distribution of the shear along the length of the track, an ordinary differential equation (ODE) describing the dynamics of a single mean value of the shear displacement along length of the track were derived. The main feature of this study is the adoption of a modelling and simulation environment, MOSES, based on object-oriented tools and techniques (Maffezzoni and Girelli, 1998).

In this work a 3D, multibody dynamic model of an agricultural robot with flexible tracks is developed in the modelling language Modelica (Mattsson et al., 1998), which is an object-oriented, declarative, multi-domain modelling language for component-oriented modelling of complex systems. The Modelica language greatly helps a modular, acausal approach to modelling, which is necessary when discretizing the system into its components (the assembly is performed by the software).

The developed model, consisting of about 300 000 equations and variables, considers both soft and hard grounds, and is contained in an open-source package. In particular, each flexible rubber track belt was modelled with a finite volumes approach by dividing it into 80

Fig. 1. AGILEX BUNKER PRO.

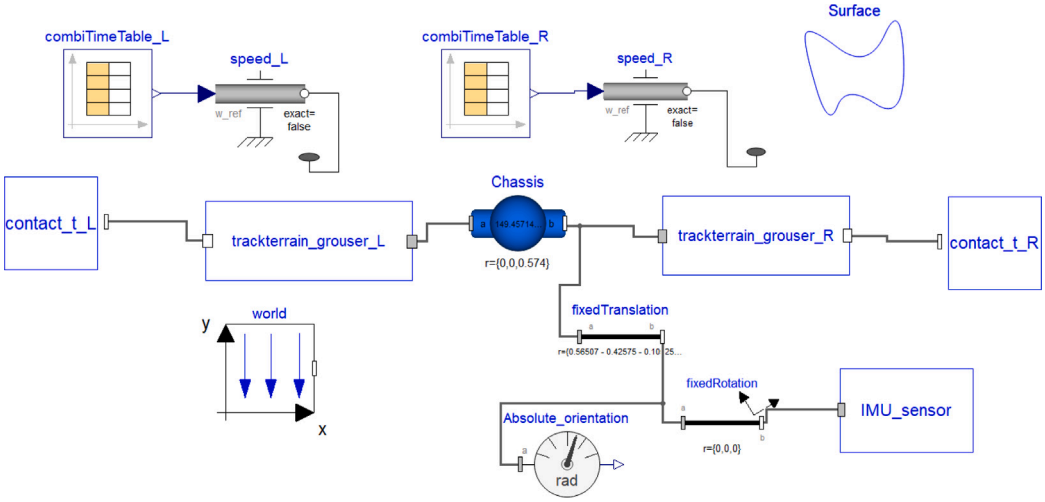

Fig. 2. Model top level.

discrete segments,[1] each discrete element is in turn divided along the transversal direction into two parts. Thanks to the modular approach enabled by the Modelica language, the complete suspension system as well as the interaction of tracks and grousers with the terrain (terramechanics) have been described with a high degree of accuracy.

The most popular Modelica-based simulation environments are Dymola (Dempsey, 2006) and OpenModelica (Fritzson et al., 2020), the last one is open-source while Dymola is commercial. In this work, the Dymola software was used as, for huge systems of equations, it is more numerically efficient than OpenModelica (Dahlquist et al., 2013; Dorado-Rojas et al., 2020), especially during the compilation phase. Furthermore, Dymola allows parallelization to increase computational efficiency (Elmqvist et al., 2014).

Today many different models and simulation environments are available, but only a few of them are suitable to accurately describe the motion of a tracked vehicle on a realistic agricultural soil, as done by the one here described. Though in many situations a simplified simulation of the vehicle, exploiting a skid-steering kinematic model, is sufficient, there are also important applications where an accurate model is needed. Among many, it is important to mention the development and validation of state estimators (e.g., slip estimators), the validation of model-based trajectory tracking controllers (e.g., MPC controllers or feedback linearizing controllers) especially in the case of complex scenarios (e.g., driving through sloping or low-friction terrains), the optimization of the design of the locomotion system and its validation, and the assessment of the changes to the soil hydraulic and mechanical properties produced by the tracks.

The aim of this work is thus to propose a modular, efficient, and accurate dynamic model of a tracked vehicle for agricultural applications that is able to support all these activities.

An extensive campaign of validation experiments has been carried out, mainly focused on the steering dynamics: on a rigid surface in indoor experiments, and on a deformable surface in outdoor experiments. In indoor experiments the actual position of the robot center of mass and its angular orientation were measured very accurately through a VICON motion capture system and an Inertial Measurement Unit (IMU), in outdoor experiments the motion capture system was replaced by a Real-Time Kinematic (RTK) Global Positioning System (GPS).

The paper is organized as follows. Section 2 first introduces the hierarchical modular structure of the model, then goes into the details describing the suspension model and the interaction of the track with the suspensions on one side, and with ground on the other side. Section 3 illustrates some validation experiments, both indoor on

[1] The subdivision in finite elements of the track belt can be done for an arbitrary number of elements, and it is not constrained by the number of grousers.

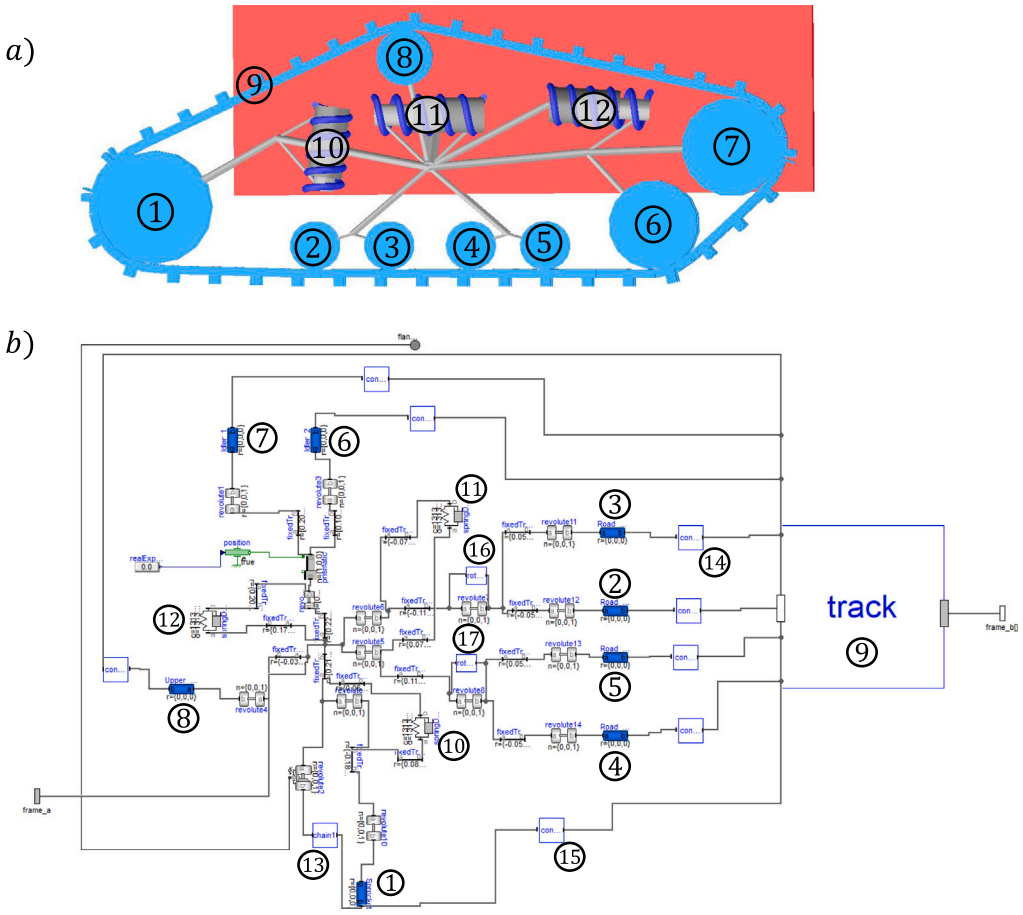

Fig. 3. Track suspension system model.

rigid ground and outdoor on deformable ground. Section 4 draws some conclusions and foresees some extensions and possible applications.

2. Model of the tracked vehicle

The tracked vehicle considered in this work is the AGILEX BUNKER PRO (Fig. 1 shows the robot equipped with the animal feeding tool and with a Light Detection and Ranging (LiDAR) sensor used for navigating in barns), a heavy-duty robot boasting a high IP67 rating, endowed with a multi-link advanced suspension system and reinforced shocks and able to move in difficult environments such as soft terrains, steep slopes, puddles.

The model has been developed in Dymola (Dempsey, 2006), a component based modelling and simulation tool based on Modelica (Mattsson et al., 1998), an object-oriented, equation based modelling language that enables component and system models to be defined in a general way without considering the causality required in a particular simulation problem.

Furthermore, the model was developed in a hierarchical way, and the top level (Fig. 2) is made by the following (sub)models (objects), all connected through multibody connectors:

- `Chassis`: instance of the `bodyshape` (rigid body) class of the Modelica Standard Library (MSL);
- `Absolute_orientation`: model extracting the absolute orientation of the robot;
- `IMU`: model of the Inertial Measurement Unit;
- `trackterrain_grouser_R` and `trackterrain_grouser_L`: models of the track suspension system for the right and left track, respectively;
- `contact_t_R` and `contact_t_L`: models of the track-terrain interaction;
- `Surface`: model describing the terrain elevation and defining the physical proprieties of the terrain;
- `world`: model defining the absolute reference frame and the gravity field.

Finally, the two `CombiTimeTable` blocks on the top are used to impose on the angular velocities of the right and left sprocket the values recorded on the real robot during the validation experiments.

Most of the geometric parameters were taken from the CAD model of the robot, apart form few ones obtained from direct measurements. The computation of all masses and inertia tensors was performed considering the total mass of the robot reported in the user manual, the total mass of the rubber track, the density of wheel material, the density of the vulcanized rubber of the track, the total number of elements of the discretized track, and the total number of grousers.

The main sub models will be illustrated in the following subsections.

2.1. Track suspension system model

The components of the model of the track suspension system (models `trackterrain_grouser_R` and `trackterrain_grouser_L`) are summarized in Fig. 3a, while Fig. 3b shows the relevant Modelica scheme.

Models numbered from 1 to 8, relevant to sprocket, wheels and idlers, are instances of the `bodyshape` class of the MSL multibody package, as well as the rotational joints connecting them to the chassis, and the models from 10 to 12, modelling suspension springs. Model 13 describes the chain transmission system between the DC servomotor

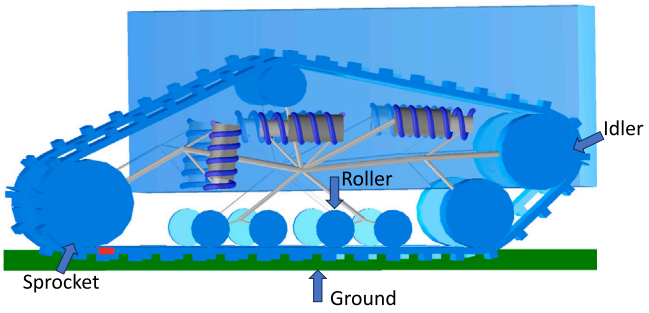

Fig. 4. Track.

and the shaft of the sprocket, while models 16 and 17 describe the rotational stops that act on the two carts of the road wheels.

The suspension stiffness values were obtained from data-sheets, the damping coefficients were set as the value of the stiffness divided by ten, while the un-stretched lengths of the springs were derived by comparing the real and simulated pose of the robot at rest.

Models 14,[2] 15, described in the next subsections, define the contact between the rolling bodies (idlers, wheels and sprocket) and the discretized track model defined by component 9.

It can be pointed out that, since the track has been discretized into several elements, the multibody connectors connecting models 14, 15 to model 9 are vector connectors, connecting the rolling bodies to all elements of the track.

2.2. Track model

The track has been modelled with a finite volume approach, where each volume, depicted in red in Fig. 4 and from now on called *element*, represents a section of the track and it is considered as a rigid body.

Each element exchanges a system of forces/torques with the adjacent elements and with the ground, sprocket, idler and rollers (blue arrows in Fig. 4), and has 4 connectors (Fig. 5). Two connectors, W, E, are used to model the exchange of elastic forces along the track, connector N is used to model the exchange of forces with rolling elements, while connector S is used to model the contact with ground. Model `bodyShape` accounts for element's mass properties, while model `bush_element` implements the exchange of elastic forces between two elements. Models `fixedTranslation2` and `grouser1` are conditional components, thus they are conditionally instantiated only when a section of the grouser is attached to the element (`there_is_grouser = true`).

The frames (O_A, $\mathbf{x}_A$, $\mathbf{y}_A$, $\mathbf{z}_A$) and (O_B, $\mathbf{x}_B$, $\mathbf{y}_B$, $\mathbf{z}_B$) of connectors A and B of the bush element have their origin in the middle of the section of adjacent elements (Fig. 6), each section having a height of h and a width of b, while the length is l.

The balance of forces and torques is defined as:

$$\begin{aligned} {}^{A}\mathbf{f}_A + {}^{A}\mathbf{A}_B\,{}^{B}\mathbf{f}_B &= \mathbf{0} \\ {}^{A}\mathbf{t}_A + {}^{A}\mathbf{A}_B\,{}^{B}\mathbf{t}_B + \boldsymbol{\delta} \times {}^{A}\mathbf{A}_B\,{}^{B}\mathbf{f}_B &= \mathbf{0} \end{aligned} \tag{1}$$

where ${}^{A}\mathbf{f}_A$, ${}^{A}\mathbf{t}_A$ and ${}^{B}\mathbf{f}_B$, ${}^{B}\mathbf{t}_B$ are the forces and torques exerted at connectors, ${}^{A}\mathbf{A}_B$ is the rotation matrix from frame B to frame A, and $\boldsymbol{\delta}$ is the deformation vector from frame A to frame B:

$$\boldsymbol{\delta} = {}^{A}\mathbf{A}_B\,{}^{B}\mathbf{p}_B - {}^{A}\mathbf{p}_A$$

${}^{A}\mathbf{p}_A$ and ${}^{B}\mathbf{p}_B$ are the vector positions, referred to the frames A and B respectively, from the origin of the absolute frame to the origins of frames A and B, respectively. However, the contribution of $\boldsymbol{\delta}$ in (1) is neglected.

The elastic forces/torques are defined as in (Qin et al., 2014):

$${}^{A}\mathbf{f}_A = -\mathrm{diag}(K_x, K_y, K_z)\boldsymbol{\delta} - \mathrm{diag}(D_x, D_y, D_z)\dot{\boldsymbol{\delta}}$$

[2] Only one is denoted for the sake of clarity.

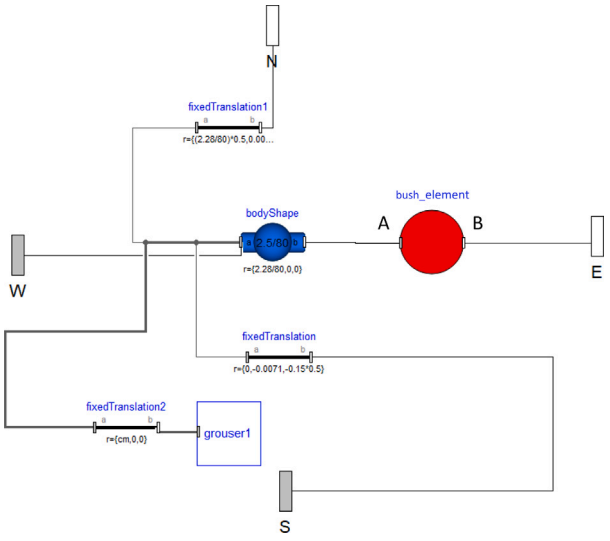

Fig. 5. Element model.

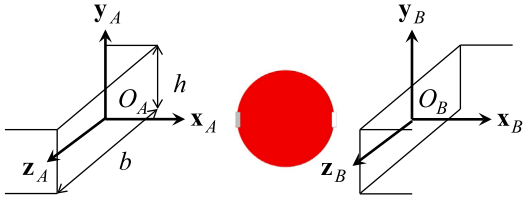

Fig. 6. Bush element frames.

$${}^{A}\mathbf{t}_A = -\left(\mathbf{T}_b(\boldsymbol{\theta}_b)^{-1}\right)^T \left[\mathrm{diag}(K_\alpha, K_\beta, K_\gamma)\boldsymbol{\theta}_b + \mathrm{diag}(D_\alpha, D_\beta, D_\gamma)\dot{\boldsymbol{\theta}}_b\right]$$

where K_i and D_i are the stiffness and damping parameters,

$$\boldsymbol{\theta}_b = \begin{bmatrix}\alpha_b & \beta_b & \gamma_b\end{bmatrix}^T$$

is the vector of the Cardan angles between the frames, and $\mathbf{T}_b(\boldsymbol{\theta}_b)$ is the transformation matrix defined in (2). In particular, the stiffness parameters can be calculated as:

$$\begin{aligned} K_x &= \frac{EA}{l} = \frac{Ehb}{l} \\ K_y &= K_z = \frac{GA}{l} = \frac{Ghb}{l} \\ K_\alpha &= \frac{3Gbh^3}{l} \\ K_\beta &= \frac{EI_y}{l} = \frac{Ehb^3}{12l} \\ K_\gamma &= \frac{EI_z}{l} = \frac{Ebh^3}{12l} \end{aligned}$$

where E is the Young's modulus, G is the shear modulus, A is the area of the element section, I_y is the moment of inertia around y axis, while I_z is the moment of inertia around $\mathbf{z}$ axis.

The rotation matrix ${}^{A}\mathbf{A}_B$ can be expressed as:

$${}^{A}\mathbf{A}_B = \mathbf{R}_x(\alpha_b)\mathbf{R}_y(\beta_b)\mathbf{R}_z(\gamma_b)$$

with $\mathbf{R}_x(\alpha_b)$, $\mathbf{R}_y(\beta_b)$, $\mathbf{R}_z(\gamma_b)$ being the basic rotation matrices along $\mathbf{x}$, $\mathbf{y}$, $\mathbf{z}$ axis. The Cardan angles $\boldsymbol{\theta}_b$ can be computed by considering the relation between the time derivative $\dot{\boldsymbol{\theta}}_b$ and the angular velocity ${}^{A}\boldsymbol{\omega}_{AB}$ of frame B with respect to frame A, referred to frame A:

$${}^{A}\boldsymbol{\omega}_{AB} = \begin{bmatrix} 1 & 0 & \sin\beta_b \\ 0 & \cos\alpha_b & -\sin\alpha_b\cos\beta_b \\ 0 & \sin\alpha_b & \cos\alpha_b\cos\beta_b \end{bmatrix}\dot{\boldsymbol{\theta}}_b = \mathbf{T}_b(\boldsymbol{\theta}_b)\dot{\boldsymbol{\theta}}_b \tag{2}$$

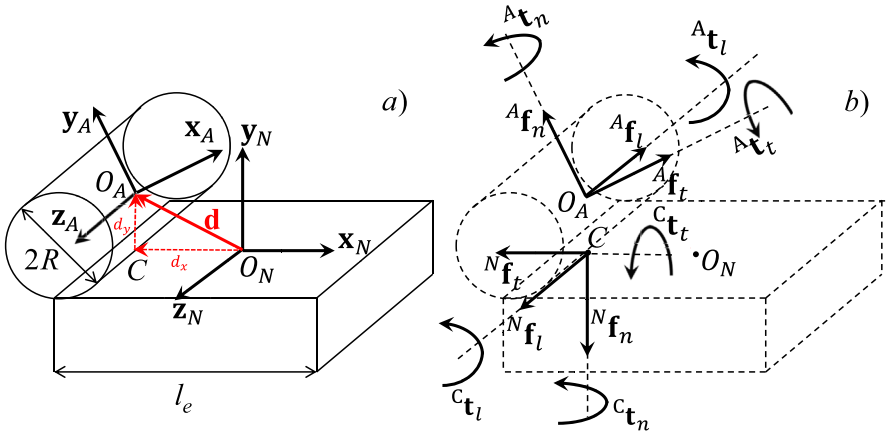

Fig. 7. Track-sprocket and track-idler contact.

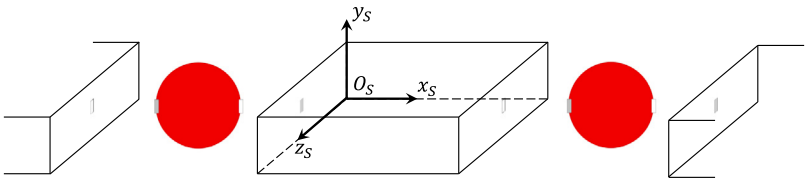

Fig. 8. Position of frame S.

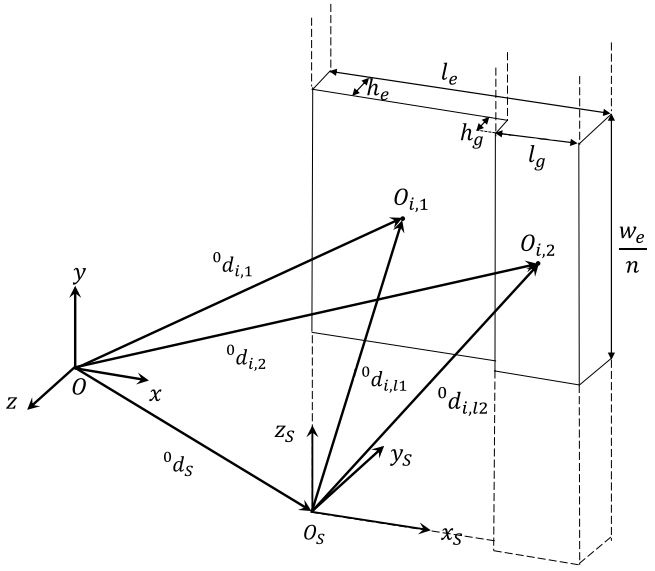

Fig. 9. Track sub-element.

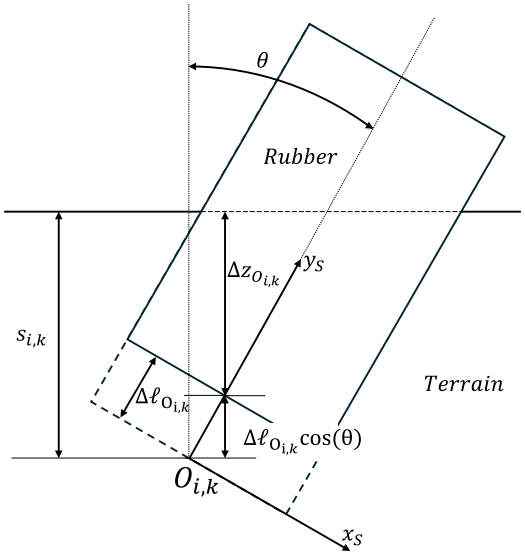

Fig. 10. Deformation of the track element and terrain.

since $\det \mathbf{T}_b(\boldsymbol{\theta}_b) = \cos\beta_b$ and the angles α_b and β_b are small, $\dot{\boldsymbol{\theta}}_b$ can be always computed from (2) and the Cardan angles $\boldsymbol{\theta}_b$ can be computed by integration (Boudon et al., 2019):

$$\dot{\boldsymbol{\theta}}_b = \mathbf{T}_b(\boldsymbol{\theta}_b)^{-1} \left({}^A\mathbf{A}_B\, {}^B\boldsymbol{\omega}_{AB}\right)$$

where the product ${}^A\mathbf{A}_B\, {}^B\boldsymbol{\omega}_{AB}$ is the angular velocity ${}^A\boldsymbol{\omega}_{AB}$ of frame B with respect to frame A, referred to frame A, and ${}^B\boldsymbol{\omega}_{AB}$ is the angular velocity of frame B with respect to frame A, referred to frame B, that can be computed from the absolute angular velocities ${}^0\boldsymbol{\omega}_A$ and ${}^0\boldsymbol{\omega}_B$ of frames A and B, respectively, in this way:

$${}^B\boldsymbol{\omega}_{AB} = {}^B\mathbf{A}_0 \left({}^0\boldsymbol{\omega}_B - {}^0\boldsymbol{\omega}_A\right)$$

where ${}^B\mathbf{A}_0$ is the rotation matrix from the absolute frame to frame B.

2.3. Model of the contact between rolling elements and track

The contact is identified by the relative distance between the origin of the frame N (O_N, $\mathbf{x}_N$, $\mathbf{y}_N$, $\mathbf{z}_N$) of the connector N depicted in Fig. 5 and attached to the element in the center of the upper surface, and the origin of the frame A (O_A, $\mathbf{x}_A$, $\mathbf{y}_A$, $\mathbf{z}_A$) of the connector A, attached to the rotating element in the center of the rotation axis, referred to frame N (Fig. 7a):

$$\mathbf{d} = {}^N\mathbf{A}_0({}^0\mathbf{p}_A - {}^0\mathbf{p}_N)$$

where ${}^N\mathbf{A}_0$ is the rotation matrix from the absolute frame to frame N, while ${}^0\mathbf{p}_A$ and ${}^0\mathbf{p}_N$ are the vector positions from the origin of the absolute frame to the origins of frames A and N respectively, both are referred to the absolute frame. In particular, contact holds when

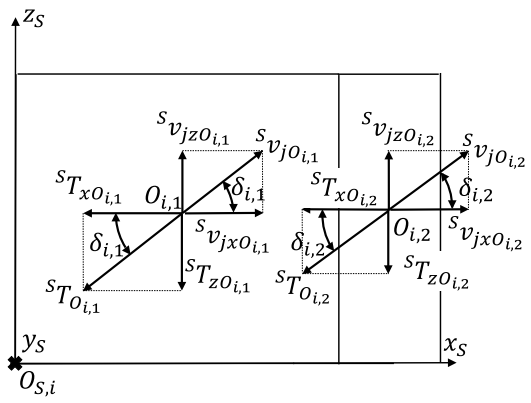

Fig. 11. Shear forces.

$$\begin{cases} |d_x| = |\mathbf{d} \cdot {}^{N}\mathbf{x}_N| \le l_e/2 \\ |d_y| = |\mathbf{d} \cdot {}^{N}\mathbf{y}_N| \le R \end{cases}$$

with l_e being the length of the element and R the radius of the rolling component. However, instead of resorting to conditional models while avoiding numerical chattering, the contact is modelled by multiplying the expression of the contact forces (see below) by a smoothing function $s(|d_x|, |d_y|)$:

$$s(|d_x|, |d_y|) = \frac{\tanh\left(-\kappa(|d_y| - R)\right) + 1}{2} \frac{\tanh\left(-\kappa(|d_x| - l_e/2)\right) + 1}{2}$$

where parameter κ is selected according to a trade-off between efficiency and accuracy, in this case $\kappa = 10^3$.

Fig. 7b shows the contact forces and torques acting on the origin of frame N, the forces and torques acting on the origin of frame A are given by the balances of forces and torques defined by (3) and (4).

The normal force ${}^{N}\mathbf{f}_n$ acting on the origin of frame N, with reference to frame N, is given by:

$$\begin{aligned} {}^{N}\mathbf{f}_n &= -f_n {}^{N}\mathbf{y}_N \\ &= -s(|d_x|, |d_y|) \max\left[0, -\left(K_n(d_y - R) + D_n \dot{d}_y\right)\right] {}^{N}\mathbf{y}_N \end{aligned}$$

In the case of track-idler contact (model `contact`), the tangential force ${}^{N}\mathbf{f}_t$ acting on the origin of frame N, with reference to frame N, is the friction force:

$${}^{N}\mathbf{f}_t = \mu(|v_r|) f_n \text{sign}(v_r) {}^{N}\mathbf{x}_N$$

while, in the case of track-sprocket contact (model `contact_sprocket`), the tangential force ${}^{N}\mathbf{f}_t$ is given by:

$${}^{N}\mathbf{f}_t = s(|d_x|, |d_y|) D_t v_r {}^{N}\mathbf{x}_N$$

where v_r is the relative velocity at the contact point along $\mathbf{x}_N$ axis:

$$v_r = {}^{N}\mathbf{x}_N \cdot \left\{ {}^{N}\mathbf{A}_0 \left[{}^{0}\mathbf{v}_A - {}^{0}\mathbf{A}_N \left(R {}^{N}\mathbf{y}_N \right) \times {}^{0}\boldsymbol{\omega}_A - {}^{0}\mathbf{v}_N \right] \right\}$$

${}^{0}\mathbf{v}_A$, ${}^{0}\boldsymbol{\omega}_A$ and ${}^{0}\mathbf{v}_N$ are the linear and angular velocities of frame A, and the linear velocity of frame N, respectively, ${}^{0}\mathbf{A}_N$ is the rotation matrix from frame N to the absolute frame, R is the radius of the rolling component, K_n and D_n are stiffness and damping parameters along the normal direction, D_t is the damping parameter along the tangential direction that assumes very high values in order to model the absence of sliding at the contact point in the case of track-sprocket contact, and $\mu(|v_r|)$ is the function considered for the friction coefficient (Oestersötebier et al., 2014):

$$\mu(|v_r|) = \gamma_1 \left(\tanh(\gamma_2 |v_r|) - \tanh(\gamma_3 |v_r|) \right) + \gamma_4 \tanh(\gamma_5 |v_r|) + \gamma_6 |v_r|$$

The lateral force ${}^{N}\mathbf{f}_l$ acting on the origin of frame N, referred to frame N, is computed as:

$${}^{N}\mathbf{f}_l = s(|d_x|, |d_y|) \left(K_l d_z + D_l \dot{d}_z \right) {}^{N}\mathbf{z}_N$$

with $d_z = \mathbf{d} \cdot {}^{N}\mathbf{z}_N$, while K_l and D_l are stiffness and damping parameters. The torques ${}^{N}\mathbf{t}_t$, ${}^{N}\mathbf{t}_n$ and ${}^{N}\mathbf{t}_l$ acting on the origin of frame N, referred to frame N, are computed as (see Fig. 7):

$$\begin{aligned} {}^{N}\mathbf{t}_t &= {}^{C}\mathbf{t}_t \\ {}^{N}\mathbf{t}_n &= {}^{C}\mathbf{t}_n + (d_x {}^{N}\mathbf{x}_N) \times {}^{N}\mathbf{f}_l \\ {}^{N}\mathbf{t}_l &= {}^{C}\mathbf{t}_t + (d_x {}^{N}\mathbf{x}_N) \times {}^{N}\mathbf{f}_n \end{aligned}$$

where ${}^{C}\mathbf{t}_t$, ${}^{C}\mathbf{t}_n$ and ${}^{C}\mathbf{t}_l$ are the contact torques acting on the contact point C (the orientation of the frame centred in C coincides with the orientation of frame N) (Qin et al., 2014):

$$\begin{bmatrix} {}^{C}\mathbf{t}_t \\ {}^{C}\mathbf{t}_n \\ {}^{C}\mathbf{t}_l \end{bmatrix} = \left(\mathbf{T}_t(\boldsymbol{\theta}_t)^{-1} \right)^T \begin{bmatrix} s(|d_x|, |d_y|) \left(K_x \alpha_t + D_x \dot{\alpha}_t \right) \\ s(|d_x|, |d_y|) \left(K_y \beta_t + D_y \dot{\beta}_t \right) \\ 0 \end{bmatrix}$$

the vector $\boldsymbol{\theta}_t = \begin{bmatrix} \alpha_t & \beta_t & \gamma_t \end{bmatrix}^T$ is the vector of the Cardan angles defining the orientation of frame A with respect to frame N, and the matrix $\mathbf{T}_t(\boldsymbol{\theta}_t)$ is the transformation matrix that maps $\dot{\boldsymbol{\theta}}_t$ to the angular velocity ${}^{N}\boldsymbol{\omega}_{NA}$ of frame A with respect to frame N, referred to frame N. Since α_t and β_t are small angles and $\det(\mathbf{T}_t(\boldsymbol{\theta}_t)) = \cos\beta_t$, the vector $\dot{\boldsymbol{\theta}}_t$ can be always computed from the mapping:

$${}^{N}\boldsymbol{\omega}_{NA} = \begin{bmatrix} 1 & 0 & \sin\beta_t \\ 0 & \cos\alpha_t & -\sin\alpha_t \cos\beta_t \\ 0 & \sin\alpha_t & \cos\alpha_t \cos\beta_t \end{bmatrix} \dot{\boldsymbol{\theta}}_t = \mathbf{T}_t(\boldsymbol{\theta}_t) \dot{\boldsymbol{\theta}}_t$$

and the Cardan angles can be computed by integration as in (Boudon et al., 2019):

$$\dot{\boldsymbol{\theta}}_t = \mathbf{T}_t(\boldsymbol{\theta}_t)^{-1} \left({}^{N}\mathbf{A}_A {}^{A}\boldsymbol{\omega}_{NA} \right)$$

where the product ${}^{N}\mathbf{A}_A {}^{A}\boldsymbol{\omega}_{NA}$ is the angular velocity ${}^{N}\boldsymbol{\omega}_{NA}$ of frame A with respect to frame N, referred to frame N, and ${}^{A}\boldsymbol{\omega}_{NA}$ is the angular velocity of frame A with respect to frame N, referred to frame A, that can be computed from the absolute angular velocities ${}^{0}\boldsymbol{\omega}_N$ and ${}^{0}\boldsymbol{\omega}_A$ of frames N and A, respectively, in this way:

$${}^{A}\boldsymbol{\omega}_{NA} = {}^{A}\mathbf{A}_0 \left({}^{0}\boldsymbol{\omega}_A - {}^{0}\boldsymbol{\omega}_N \right)$$

where ${}^{A}\mathbf{A}_0$ is the rotation matrix from the absolute frame to frame A.

The forces and torques acting on the origin of frame A, referred to frame A, can be computed from the following balance of forces and torques:

$${}^{A}\mathbf{f}_A + {}^{A}\mathbf{A}_N {}^{N}\mathbf{f}_N = \mathbf{0} \tag{3}$$

$${}^{A}\mathbf{t}_A + {}^{A}\mathbf{A}_N \begin{bmatrix} {}^{C}\mathbf{t}_t - (R {}^{N}\mathbf{y}_N) \times {}^{N}\mathbf{f}_l & {}^{C}\mathbf{t}_n & (R {}^{N}\mathbf{y}_N) \times {}^{N}\mathbf{f}_t \end{bmatrix}^T = \mathbf{0} \tag{4}$$

where R is the radius of the rolling component and ${}^{A}\mathbf{A}_N$ is the rotation matrix from frame N to frame A, defined as:

$${}^{A}\mathbf{A}_N = \mathbf{R}_z(\gamma_t) \mathbf{R}_y(\beta_t) \mathbf{R}_x(\alpha_t)$$

2.4. Track-terrain interaction

The frame (O_S, $\mathbf{x}_S$, $\mathbf{y}_S$, $\mathbf{z}_S$) of the connector S introduced in Fig. 5, is located as in Fig. 8. The lower surface of the track element (rotated by 90° in Fig. 9) is divided along the $\mathbf{z}_S$ axis in n parts, and for each area two vectors, ${}^{0}\mathbf{d}_{i,1}$ and ${}^{0}\mathbf{d}_{i,2}$, are computed, namely the vector positions from the origin of the absolute frame to the points $O_{i,1}$ and $O_{i,2}$, respectively, both referred to the absolute frame, with $O_{i,1}$ being the center of the area not occupied by the grouser, and $O_{i,2}$ being the center of the contact area of the grouser:

$${}^{S}\mathbf{d}_{i,l1} = \begin{cases} \begin{bmatrix} \texttt{cm1} & 0 & w_e \frac{i-0.5}{n} \end{bmatrix}^T & \text{if } \texttt{there\_is\_grouser} \\ \begin{bmatrix} 0.5 l_e & 0 & w_e \frac{i-0.5}{n} \end{bmatrix}^T & \text{otherwise} \end{cases}$$

$${}^{S}\mathbf{d}_{i,l2} = \begin{cases} \begin{bmatrix} \texttt{cm2} & -h_g & w_e \frac{i-0.5}{n} \end{bmatrix}^T & \text{if } \texttt{there\_is\_grouser} \\ \begin{bmatrix} 0 & 0 & 0 \end{bmatrix}^T & \text{otherwise} \end{cases}$$

$$
{}^0\mathbf{d}_{i,1} = {}^0\mathbf{d}_{S,i} + {}^0\mathbf{A}_S\,{}^S\mathbf{d}_{i,l1} = {}^0\mathbf{d}_{S,i} + {}^0\mathbf{d}_{i,l1}
$$

$$
{}^0\mathbf{d}_{i,2} = \begin{cases} {}^0\mathbf{d}_{S,i} + {}^0\mathbf{A}_S\,{}^S\mathbf{d}_{i,l2} = {}^0\mathbf{d}_{S,i} + {}^0\mathbf{d}_{i,l2} & \text{if } \texttt{there\_is\_grouser} \\ \begin{bmatrix} 0 & 0 & 0 \end{bmatrix}^T & \text{otherwise} \end{cases}
$$

where the parameters `cm1` and `cm2` are the coordinates of the points $O_{i,1}$ and $O_{i,2}$ in frame S along the $\mathbf{x}_S$ axis, the parameter `there_is_grouser` is a boolean parameter equal to `true` if the track element includes the grouser, `false` otherwise, ${}^0\mathbf{A}_S$ is the rotation matrix from frame S to the absolute frame, w_e and l_e are the width and the length of the track element, and h_g is the height of the grouser (Fig. 9).

The contact condition for point $O_{i,k}$ $(k = 1, 2)$ is identified by the sign of the sinkage $s_{i,k}$:

$$
s_{i,k} = f_e\left({}^0\mathbf{d}_{i,k} \cdot {}^0\mathbf{x}_0, {}^0\mathbf{d}_{i,k} \cdot {}^0\mathbf{z}_0\right) - {}^0\mathbf{d}_{i,k} \cdot {}^0\mathbf{y}_0 \quad , \quad k = 1, 2
$$

where f_e is a function that returns the elevation of the surface at point $O_{i,k}$ (see next subsection).

It is now possible to define the speeds of slip $v_{xOi,k}$ and $v_{zOi,k}$, and the shear displacements $j_{xOi,k}$ and $j_{zOi,k}$ of points $O_{i,k}$, assuming that both are in contact with ground:

$$
\begin{aligned}
v_{xO_{i,k}} &= \frac{\mathrm{d}\left({}^0\mathbf{d}_{i,k}\right)}{\mathrm{d}t} \cdot {}^0\mathbf{x}_S \quad , \quad k = 1, 2 \\
v_{zO_{i,k}} &= \frac{\mathrm{d}\left({}^0\mathbf{d}_{i,k}\right)}{\mathrm{d}t} \cdot {}^0\mathbf{z}_S \quad , \quad k = 1, 2 \\
j_{xO_{i,k}} &= \int_{\bar{t}_{i,k}}^{t} v_{jxO_{i,k}}(\tau)\,\mathrm{d}\tau \quad , \quad k = 1, 2 \\
j_{zO_{i,k}} &= \int_{\bar{t}_{i,k}}^{t} v_{jzO_{i,k}}(\tau)\,\mathrm{d}\tau \quad , \quad k = 1, 2
\end{aligned}
$$

where $\bar{t}_{i,k}$ is the time instant in which contact is established between point $O_{i,k}$ and ground. To reset the value of the shear displacements to zero when contact is lost ($s_{i,k} = 0$), the Modelica `reinit` operator could be used. However, since an excessive slowdown of the simulation was experienced, it was preferred to reset to zero the shear displacement through a very fast dynamics:

$$
\begin{aligned}
\frac{\mathrm{d}\left(j_{xO_{i,k}}\right)}{\mathrm{d}t} &= -\kappa_j j_{xO_{i,k}} \quad , \quad k = 1, 2 \\
\frac{\mathrm{d}\left(j_{zO_{i,k}}\right)}{\mathrm{d}t} &= -\kappa_j j_{zO_{i,k}} \quad , \quad k = 1, 2
\end{aligned}
$$

with $\kappa_j = 1000$.

The total sinkage $s_{i,k}$ of point $O_{i,k}$ is the sum of two terms (Fig. 10): $\Delta z_{O_{i,k}}$, the sinkage of the deformed rubber element, and $\Delta l_{O_{i,k}} \cos(\theta)$, representing the deformation of the rubber element of the track, with $\cos(\theta)$ being the cosine of the angle between ${}^0\mathbf{y}_0$ and ${}^0\mathbf{y}_S$:

$$
s_{i,k} = \Delta z_{O_{i,k}} + \Delta l_{O_{i,k}} \cos(\theta)
$$

In turn, both terms $\Delta z_{O_{i,k}}$ and $\Delta l_{O_{i,k}}$ are related to the pressures $p_{O_{i,k}}$ exerted in point $O_{i,k}$. $\Delta z_{O_{i,k}}$ through the Bekker equation (Bekker, 1969):

$$
p_{O_{i,k}} = \left(\frac{k_c}{b} + k_\phi\right) \Delta z_{O_{i,k}}^n + k_{vt} \frac{\mathrm{d}\left(\Delta z_{O_{i,k}}\right)}{\mathrm{d}t}
$$

while $\Delta l_{O_{i,k}}$ by defining a linear elastic behaviour of the rubber, introducing a compliance k_r and a damping coefficient k_{vr}:

$$
p_{O_{i,k}} = k_r \Delta l_{O_{i,k}} + k_{vr} \frac{\mathrm{d}\left(\Delta l_{O_{i,k}}\right)}{\mathrm{d}t}
$$

The physical parameters of the terrain are summarized in Table 1, where the numerical values refer to a dry sandy loam, the terrain considered for outdoor experiments (Sections 3.2.1 and 3.2.2).

Consider now the computation of the shear forces, starting from the generally accepted empirical approach proposed in Janosi and Hanamoto (1961) to relate the total shear stress τ with the total shear displacement j and the pressure p through an exponential function:

$$
\tau = \tau_{\max}(p)\left(1 - e^{-|j|/K}\right) \tag{5}
$$

where K is the shear deformation modulus, j is the total shear displacement, while the maximum shear stress $\tau_{\max}(p)$ is given by the minimum between the maximum shear strength $\tau_{\max,s}(p)$ at which the soil fail and the maximum shear strength $\tau_{\max,ts}(p)$ between the track element and

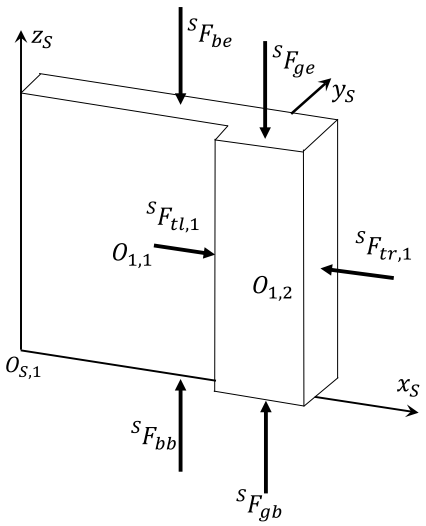

Fig. 12. Bulldozing and traction forces.

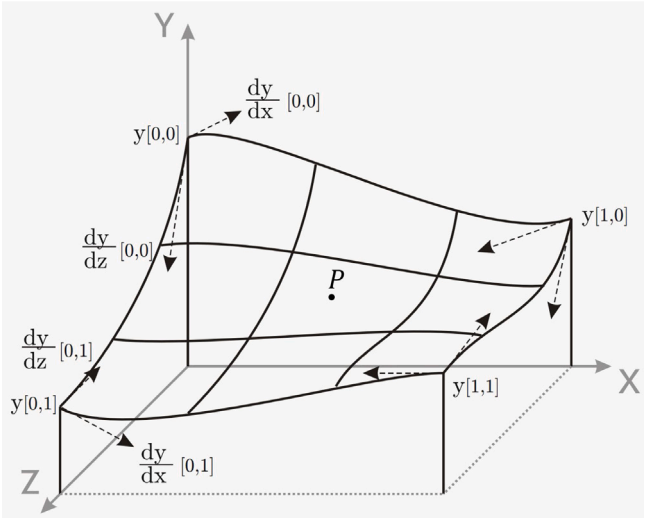

Fig. 13. Point on face.

Table 1
Parameters defining the physical properties of the terrain.

Parameter	Symbol	Unit	Value
Friction coefficient	μ_s	–	0.9
Cohesive modulus of soil deformation	k_c	N/m^{n+1}	52.53
Frictional modulus of soil deformation	k_f	N/m^{n+2}	1127.97
Exponent of soil deformation	n	–	0.9
Damping coefficient of the soil	k_{vt}	Ns/m^3	530.1
Soil cohesion	c	Pa	0
Tangent of the friction angle	$\tan(\phi)$	–	$\tan(20°)$
Shear deformation parameter	K	m	0.025
Terrain specific weight	γ_s	N/m^3	11

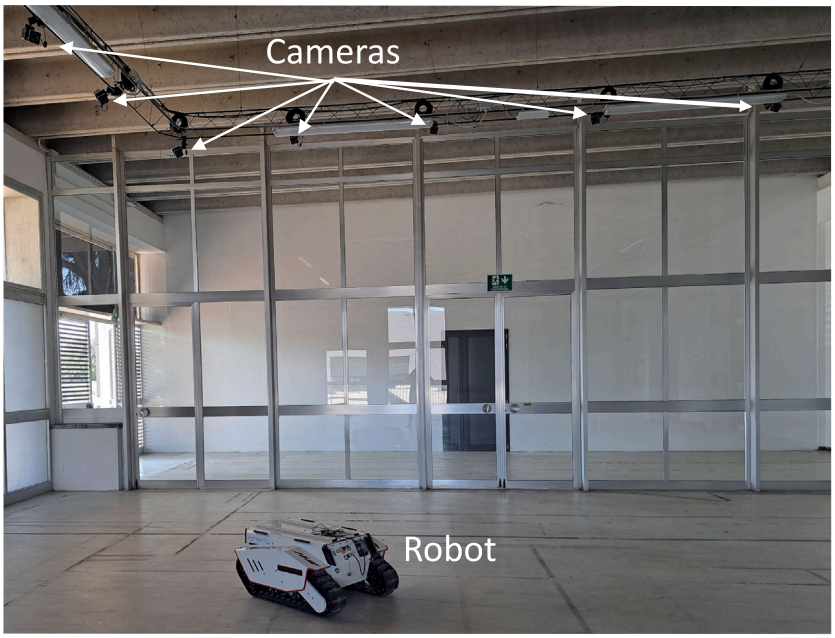

Fig. 14. Robot and VICON motion capture system.

the soil. The value of $\tau_{\max,s}(p)$ can be computed by using the Mohr–Coulomb failure criterion for which $\tau_{\max,s}(p)$ depends on the apparent cohesion of the soil c, on the pressure p and on the angle of internal shearing resistance of the soil ϕ (Wong, 2001):

$$\tau_{\max,s}(p) = c + p\tan\phi$$

while the value of $\tau_{\max,ts}(p)$ can be approximated as a function of the pressure p and of the friction coefficient μ_s:

$$\tau_{\max,ts}(p) = \mu_s p$$

the maximum shear stress $\tau_{\max}(p)$ defined in (5) is therefore (Harnisch et al., 2005):

$$\tau_{\max}(p) = \min\left(\tau_{\max,ts}(p), \tau_{\max,s}(p)\right) = \min\left(\mu_s p, c + p\tan\phi\right)$$

The computation of the total shear displacements $j_{O_{i,k}}$ $(k = 1,2)$, of the shear forces ${}^S\mathbf{T}_{xO_{i,k}}$ $(k = 1,2)$ and ${}^S\mathbf{T}_{zO_{i,k}}$ $(k = 1,2)$, and of the normal force ${}^S\mathbf{P}_{O_{i,k}}$ $(k = 1,2)$ acting on points $O_{i,k}$ $(k = 1,2)$ can be now performed based on Fig. 11 (Wong, 2001):

$$\begin{aligned}
j_{O_{i,k}} &= \sqrt{j_{xO_{i,k}}^2 + j_{zO_{i,k}}^2} \quad , \quad k = 1,2 \\
\sin\left(\delta_{i,k}\right) &= \frac{v_{jzO_{i,k}}}{\sqrt{v_{jxO_{i,k}}^2 + v_{jzO_{i,k}}^2}} \quad , \quad k = 1,2 \\
\cos\left(\delta_{i,k}\right) &= \frac{v_{jxO_{i,k}}}{\sqrt{v_{jxO_{i,k}}^2 + v_{jzO_{i,k}}^2}} \quad , \quad k = 1,2 \\
\tau_{O_{i,k}} &= \tau_{\max}\left(p_{O_{i,k}}\right)\left(1 - e^{-\frac{j_{O_{i,k}}}{K}}\right) \quad , \quad k = 1,2 \\
\tau_{xO_{i,k}} &= \tau_{O_{i,k}}\cos\left(\delta_{i,k}\right) \quad , \quad k = 1,2 \\
\tau_{zO_{i,k}} &= \tau_{O_{i,k}}\sin\left(\delta_{i,k}\right) \quad , \quad k = 1,2 \\
{}^S\mathbf{T}_{xO_{i,k}} &= -\tau_{xO_{i,k}} A_k\, {}^S\mathbf{x}_S \quad , \quad k = 1,2 \\
{}^S\mathbf{T}_{zO_{i,k}} &= -\tau_{zO_{i,k}} A_k\, {}^S\mathbf{z}_S \quad , \quad k = 1,2 \\
{}^S\mathbf{P}_{O_{i,k}} &= p_{O_{i,k}} A_k\, {}^S\mathbf{y}_S \quad , \quad k = 1,2
\end{aligned}$$

where $A_k = A_f$ if $k = 1$ (area of the surface not occupied by the grouser) while $A_k = A_g$ if $k = 2$ (area of the grouser).

Refer now to Fig. 12, where a single part for the lower surface of the track element has been considered for simplicity ($n = 1$), for the computation of the lateral forces due to the bulldozing effect, ${}^S\mathbf{F}_{be}$, ${}^S\mathbf{F}_{ge}$, ${}^S\mathbf{F}_{bb}$, and ${}^S\mathbf{F}_{gb}$, and the traction forces ${}^S\mathbf{F}_{tr,i}$ and ${}^S\mathbf{F}_{tl,i}$ due to the grousers.

Defining

$$N_\phi = \tan\left(\frac{\pi}{4} + \frac{\phi}{2}\right)^2$$

$$F_{bi,k} = \left(\frac{1}{2}\gamma_s \min\left(\frac{\Delta z_{O_{i,k}}}{\cos(\theta)}, h_e\right)^2 N_\phi + 2c \min\left(\frac{\Delta z_{O_{i,k}}}{\cos(\theta)}, h_e\right)\sqrt{N_\phi}\right) l_e$$

$$F_{gi,k} = \left(\frac{1}{2}\gamma_s \min\left(\frac{\Delta z_{O_{i,k}}}{\cos(\theta)}, h_g\right)^2 N_\phi + 2c \min\left(\frac{\Delta z_{O_{i,k}}}{\cos(\theta)}, h_g\right)\sqrt{N_\phi}\right) l_g$$

$$\begin{aligned}
F_{t,i} = \Bigg(&\frac{1}{2}\gamma_s \min\left(\frac{\Delta z_{O_{i,2}}}{\cos(\theta)}, h_g\right)^2 N_\phi + p_{O_{i,1}} \min\left(\frac{\Delta z_{O_{i,2}}}{\cos(\theta)}, h_g\right) N_\phi + \\
&+ 2c \min\left(\frac{\Delta z_{O_{i,2}}}{\cos(\theta)}, h_g\right)\sqrt{N_\phi}\Bigg)\frac{w_e}{n}\left(1 - e^{\frac{\left|j_{xO_{i,2}}\right|}{K}}\right)
\end{aligned}$$

where γ_s is the specific weight of the terrain, the lateral forces are given by (Wong, 2001):

$$\begin{aligned}
{}^S\mathbf{F}_{be} &= -F_{bn,1}\frac{\left(\text{sign}\left(v_{jzO_{n,1}}\right) + 1\right)}{2}\,{}^S\mathbf{z}_S \\
{}^S\mathbf{F}_{bb} &= F_{b1,1}\frac{\left(\text{sign}\left(-v_{jzO_{1,1}}\right) + 1\right)}{2}\,{}^S\mathbf{z}_S \\
{}^S\mathbf{F}_{ge} &= -F_{gn,2}\frac{\left(\text{sign}\left(v_{jzO_{n,2}}\right) + 1\right)}{2}\,{}^S\mathbf{z}_S \\
{}^S\mathbf{F}_{gb} &= F_{g1,2}\frac{\left(\text{sign}\left(-v_{jzO_{1,2}}\right) + 1\right)}{2}\,{}^S\mathbf{z}_S
\end{aligned}$$

while the traction forces are given by (Nicolini et al., 2018):

$${}^S\mathbf{F}_{gr,i} = \begin{cases} -F_{t,i}\frac{\left(1+\text{sign}\left(v_{jxO_{i,2}}\right)\right)}{2}\,{}^S\mathbf{x}_S & \text{if } \texttt{fr} \\ \mathbf{0} & \text{otherwise} \end{cases}$$

$${}^S\mathbf{F}_{gl,i} = \begin{cases} F_{t,i}\frac{\left(1+\text{sign}\left(-v_{jxO_{i,2}}\right)\right)}{2}\,{}^S\mathbf{x}_S & \text{if } \texttt{fl} \\ \mathbf{0} & \text{otherwise} \end{cases}$$

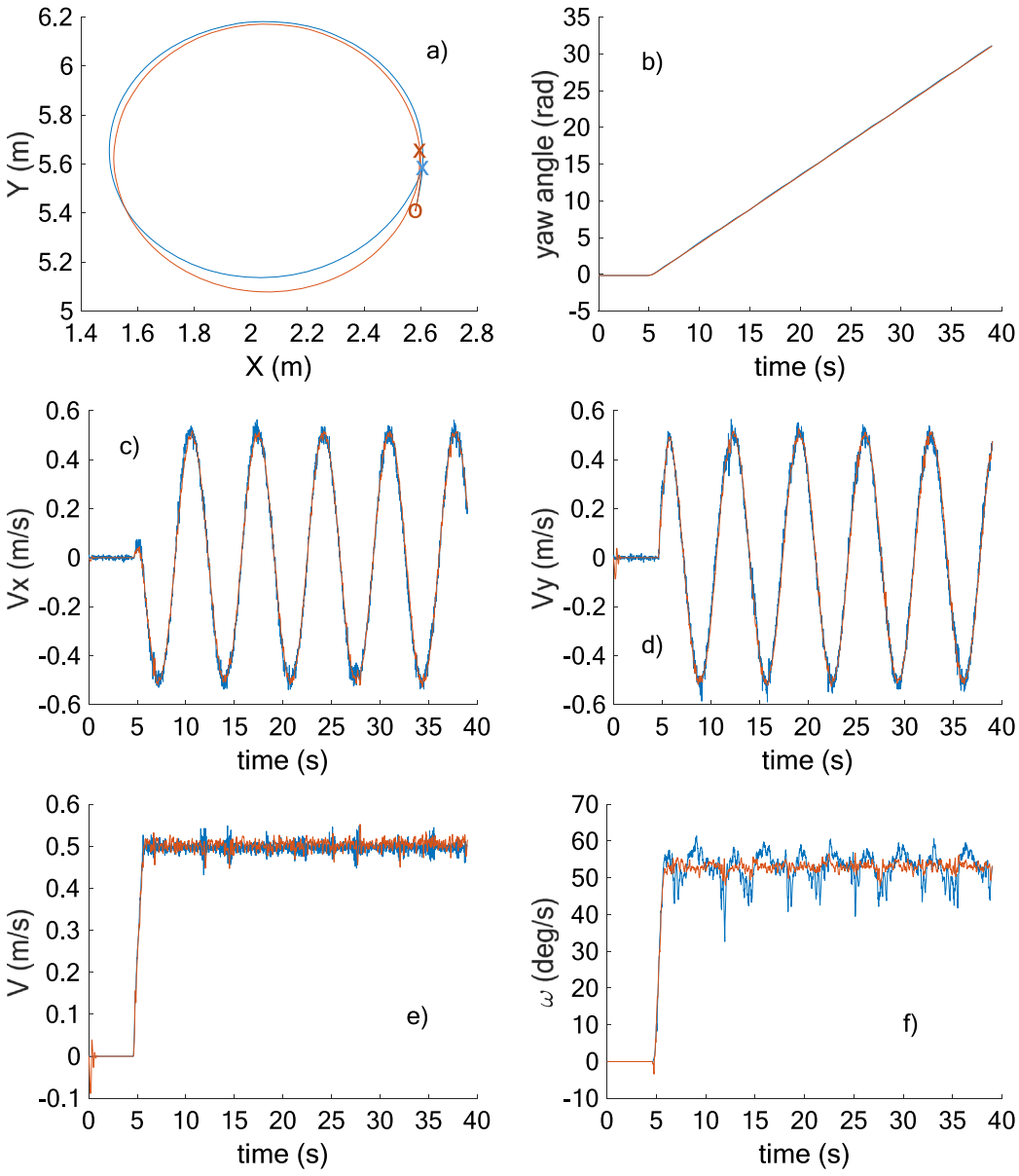

Fig. 15. Step steering: comparisons between simulations (red line) and experiments (blue line). (a) Trajectories of the center of mass in the horizontal plane (o and x denote the start and end of the trajectories); (b) yaw angle, TIC = 0.004; (c) velocity of the center of mass along the x axis, TIC = 0.039; (d) velocity of the center of mass along the y axis, TIC = 0.046; (e) linear velocity, TIC = 0.028; (f) angular velocity, TIC = 0.037.

where `fr` and `fl` are boolean parameters that are equal to `true` if the ahead and back faces of the grouser are inside the element. The values of the above forces are set to zero when a rigid terrain is considered, namely when $\Delta z_{O_{i,1}}/\cos(\theta)$ and $\Delta z_{O_{i,2}}/\cos(\theta)$ are lower or equal to 1 mm.

The total force ${}^S\mathbf{f}_S$ and torque ${}^S\mathbf{t}_S$ acting in the origin of frame S (Fig. 8) can be then calculated as follows:

$$
\begin{aligned}
{}^S\mathbf{f}_S &= \sum_{i=1}^{n} {}^S\mathbf{P}_{O_{i,1}} + \sum_{i=1}^{n} {}^S\mathbf{P}_{O_{i,2}} \\
&+ \sum_{i=1}^{n} {}^S\mathbf{T}_{xO_{i,1}} + \sum_{i=1}^{n} {}^S\mathbf{T}_{xO_{i,2}} + \sum_{i=1}^{n} {}^S\mathbf{F}_{gr,i} + \sum_{i=1}^{n} {}^S\mathbf{F}_{gl,i} \\
&+ \sum_{i=1}^{n} {}^S\mathbf{T}_{zO_{i,1}} + \sum_{i=1}^{n} {}^S\mathbf{T}_{zO_{i,2}} + {}^S\mathbf{F}_{be} + {}^S\mathbf{F}_{bb} + {}^S\mathbf{F}_{ge} + {}^S\mathbf{F}_{gb} \\
{}^S\mathbf{t}_S &= \sum_{i=1}^{n} {}^S\mathbf{d}_{i,l1} \times \left({}^S\mathbf{P}_{O_{i,1}} + {}^S\mathbf{T}_{xO_{i,1}} + {}^S\mathbf{T}_{zO_{i,1}} \right) \\
&+ \sum_{i=1}^{n} {}^S\mathbf{d}_{i,l2} \times \left({}^S\mathbf{P}_{O_{i,2}} + {}^S\mathbf{T}_{xO_{i,2}} + {}^S\mathbf{T}_{zO_{i,2}} \right) \\
&+ {}^S\mathbf{d}_{be} \times {}^S\mathbf{F}_{be} + {}^S\mathbf{d}_{bb} \times {}^S\mathbf{F}_{bb} \\
&+ {}^S\mathbf{d}_{ge} \times {}^S\mathbf{F}_{ge} + {}^S\mathbf{d}_{gb} \times {}^S\mathbf{F}_{gb} \\
&+ \sum_{i=1}^{n} {}^S\mathbf{d}_{g,i} \times \left({}^S\mathbf{F}_{gr,i} + {}^S\mathbf{F}_{gl,i} \right)
\end{aligned}
$$

where ${}^S\mathbf{d}_{be}$, ${}^S\mathbf{d}_{bb}$, ${}^S\mathbf{d}_{ge}$, ${}^S\mathbf{d}_{gb}$, and ${}^S\mathbf{d}_{g,i}$ are the local vectors position from the origin of frame S to the points of application of the forces ${}^S\mathbf{F}_{be}$, ${}^S\mathbf{F}_{bb}$, ${}^S\mathbf{F}_{ge}$, ${}^S\mathbf{F}_{gb}$, ${}^S\mathbf{F}_{gr,i}$, and ${}^S\mathbf{F}_{gl,i}$, respectively:

$$
{}^S\mathbf{d}_{be} = \left[\mathrm{cm1} \quad \min\left(\frac{\Delta z_{O_{n,1}}}{\cos(\theta)}, h_e \right) 0.5 \quad w_e \right]^T
$$

$$
{}^S\mathbf{d}_{bb} = \left[\mathrm{cm1} \quad \min\left(\frac{\Delta z_{O_{1,1}}}{\cos(\theta)}, h_e \right) 0.5 \quad 0 \right]^T
$$

$$
{}^S\mathbf{d}_{ge} = \left[\mathrm{cm2} \quad -\left(hg - \Delta l_{O_{n,2}} - \min\left(\frac{\Delta z_{O_{n,1}}}{\cos(\theta)}, hg - \Delta l_{O_{n,2}} \right) 0.5 \right) \quad w_e \right]^T
$$

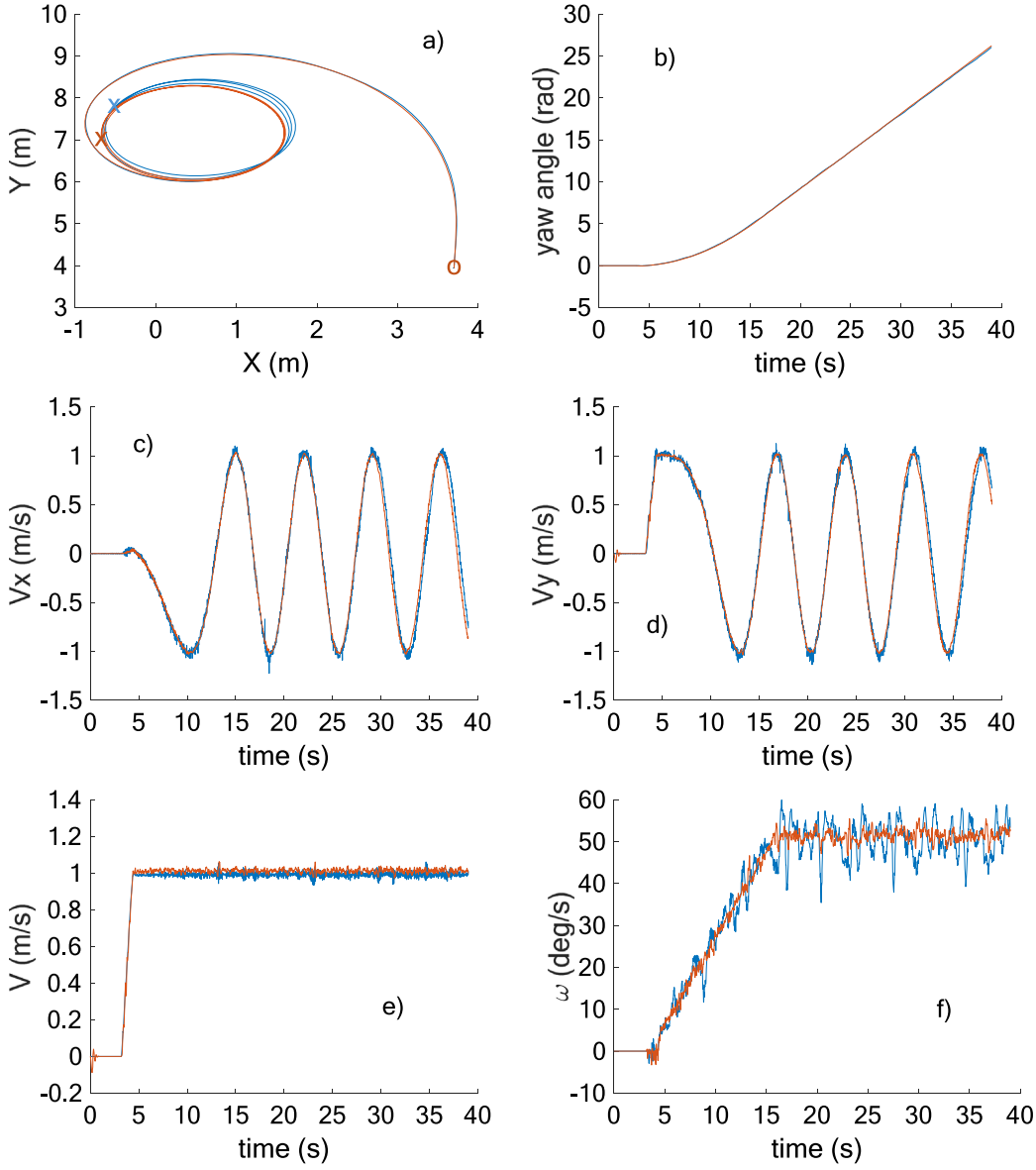

Fig. 16. Ramp steering: comparisons between simulations (red line) and experiments (blue line). (a) Trajectories of the center of mass in the horizontal plane (o and x denote the start and end of the trajectories); (b) yaw angle, TIC = 0.005; (c) velocity of the center of mass along the x axis, TIC = 0.060; (d) velocity of the center of mass along the y axis, TIC = 0.048; (e) linear velocity, TIC = 0.021; (f) angular velocity, TIC = 0.044.

$$ {}^{S}\mathbf{d}_{gb} = \left[\texttt{cm2} \quad -\left(hg - \Delta l_{O_{1,2}} - \min\left(\frac{\Delta z_{O_{1,1}}}{\cos(\theta)}, hg - \Delta l_{O_{1,2}}\right) 0.5\right) \quad 0\right]^T $$

$$ {}^{S}\mathbf{d}_{g,i} = \left[\texttt{cm2} \; -\left(hg - \Delta l_{O_{i,2}} - \min\left(\frac{\Delta z_{O_{i,1}}}{\cos(\theta)}, hg - \Delta l_{O_{i,2}}\right) 0.5\right) \; w_e \frac{i-0.5}{n}\right]^T $$

2.5. Terrain model

The geometrical and physical description of the terrain (model `Surface`) has been derived from Andres (2009), here extended to define the elevation also through analytical functions and to characterize the terramechanics.

The geometric model of the terrain is defined by meshing a surface of dimension `LengthX`×`LengthZ` into `nx`×`nz` faces, in turn, the elevation y of each point P inside each face is obtained through a cubic interpolation, based on four y values and eight directional partial derivatives in the vertices (Fig. 13). The physical parameters of the terrain (Table 1), are also defined for each face.

3. Model validation

The linear velocity V and the angular velocity ω of the robot were assigned as inputs to the robot motion controller, and the angular velocities ω_R and ω_L of the right and left sprocket were recorded from the experiments and assigned as inputs to the simulation model.[3]

The track was discretized into 80 elements with 2 divisions of the track shoe, a total number of 278 047 equations was obtained. The solver CVODE was adopted, with a tolerance of 10^{-3}, while exploiting sparsity and multi-core processing using 20 cores.

The matching between measured and simulated data was estimated by calculating the Theil's Inequality Coefficient (TIC) (Decostere et al.,

[3] Inverse dynamics computation can be directly performed in Modelica environment.

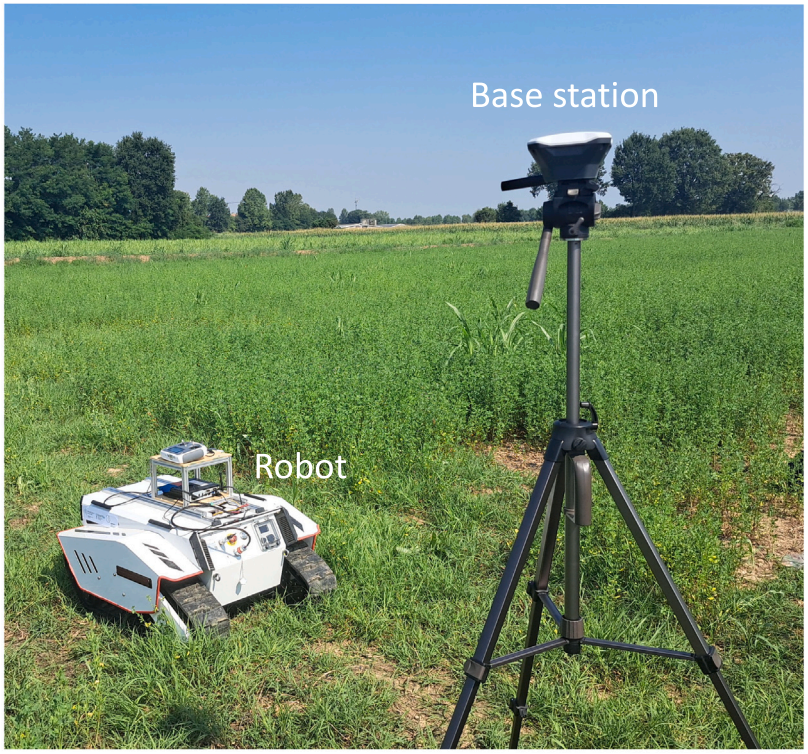

Fig. 17. Robot and GPS system.

2016) (reported in figure captions):

$$\mathrm{TIC} = \frac{\sqrt{\sum_i \left(y_i - y_{i,m}\right)^2}}{\sqrt{\sum_i y_i^2} + \sqrt{\sum_i y_{i,m}^2}} \tag{6}$$

where y_i and $y_{i,m}$ represent simulated and measured data points, respectively. A TIC value lower than 0.3 indicates a good agreement between simulation and measured data.

3.1. Indoor experiments

In indoor experiments the actual position of the robot center of mass and its angular orientation were recorded through a VICON motion capture system, consisting of 30 cameras placed on the ceiling in a rectangular perimeter of dimensions 14.8 × 7.3 m (Fig. 14). The infrared light emitted by the camera illuminators is reflected back by five retro-reflective markers placed on the robot, allowing the tracking of the robot motion at a sampling frequency of 120 frames per second, with a spatial resolution in the millimetre range.

Moreover, the acceleration and yaw rate measurements were collected through an Inertial Measurement Unit (IMU), also placed on the robot, with a sampling frequency of 100 Hz, a resolution of 5.5×10^{-5} deg/s on the yaw angular velocity, and an accuracy of 0.1 deg on the yaw angle.

A shear deformation modulus $K = 0.02$ mm and a friction coefficient $\mu_s = 0.7$ were assumed to characterize the flat, uniform, linoleum surface, all other parameters reported in Table 1 are ineffective, since the soil is rigid.

As it is apparent, a very good agreement between simulations and experiments has been obtained.

3.1.1. Step steering

In a first experiment a step to the angular velocity ω of amplitude 1 rad/s and a step to the linear velocity V of amplitude 0.5 m/s have been commanded to the robot.

Fig. 15 shows the comparisons between simulations and measurements relevant to the trajectory of the center of mass in the horizontal plane, the yaw angle, the components of the linear velocity in the horizontal plane, the linear and angular velocity (TIC values are reported in the caption).

The measured angular velocity is affected by a slight oscillation (about one degree on the angular position), less evident in the following figures and in the outdoor experiments, influenced, in addition to the measurement noise, also by the irregularities of the ground. The causes of this oscillation are currently under investigation, it is assumed that they may depend on neglected elastic dynamics of the chassis on which the IMU is fixed and on a non-perfect positioning of the IMU itself in correspondence with the center of mass.

3.1.2. Ramp steering

In a second experiment a step to the linear velocity of amplitude 1 m/s has been again applied, while a ramp from 0 to 1 rad/s has been commanded to the angular velocity, causing a spiral trajectory of the center of mass of the vehicle. Results are reported in Fig. 16.

3.2. Outdoor experiments

In outdoor experiments the actual position of the robot center of mass is measured through a RTK GPS device. Two receivers are used in RTK GPS systems, one of them is stationary and it is called *base station* (Fig. 17), the other one is fixed on the robot and it is called *rover*. By using a local base station in addition to satellite signals, the system can

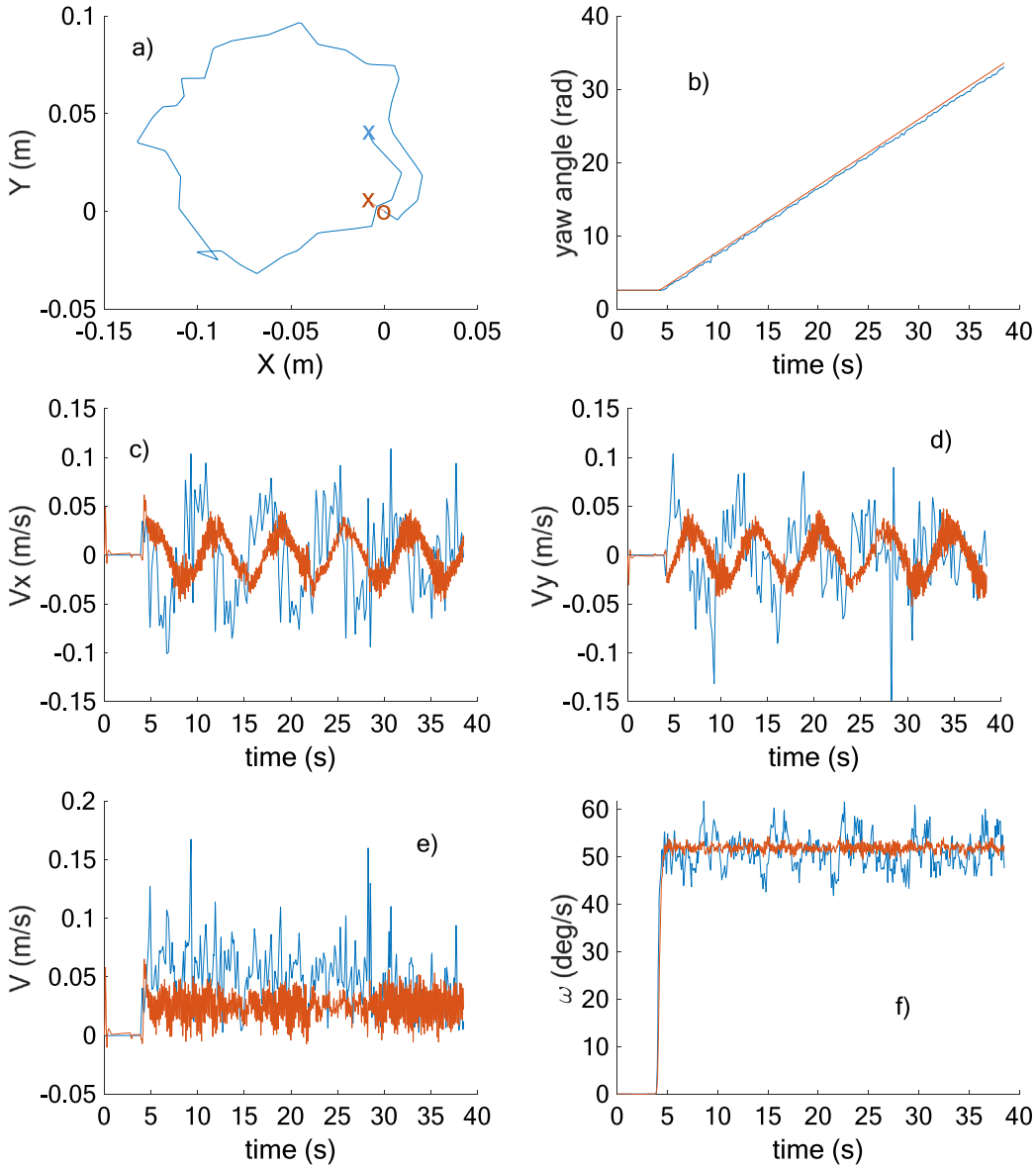

Fig. 18. Pivot turn: comparisons between simulations (red line) and experiments (blue line). (a) Trajectories of the center of mass in the horizontal plane (o and x denote the start and end of the trajectories); (b) yaw angle, TIC = 0.012; (c) velocity of the center of mass along the x axis, TIC = 0.756; (d) velocity of the center of mass along the y axis, TIC = 0.740; (e) linear velocity, TIC = 0.424; (f) angular velocity, TIC = 0.037.

correct for errors in the GPS data, by comparing the GPS data received by the base station and the GPS data received by the rover.

Measurements were collected with a sampling frequency of 5 Hz, a horizontal resolution of 7 mm + 1 ppm and a vertical resolution of 14 mm + 1 ppm. Accelerations and yaw rate measurements were collected with the same IMU used in indoor experiments.

It must be pointed out that after a single turn maneuver of the vehicle the vegetation present is completely uprooted and the soil is moved, therefore it can be assumed that the outdoor experiments were carried out on a sandy loam terrain. The values of the characteristic parameters are reported in Table 1 (see also Wong, 2001), the physical properties of the terrain were assumed to be uniform across the entire surface.

Even in outdoor experiments, a good agreement between simulations and measured data is obtained, in spite of the influence of terrain irregularities.

3.2.1. Pivot turn

In a first experiment a pivot turn is applied to the robot, namely, a zero linear velocity V has been selected, while a step of 1 rad/s has been commanded to the angular velocity ω. Results are reported in Fig. 18.

A very good agreement has been obtained with reference to the yaw angle and the linear and angular velocities. The measured trajectory of the center of mass exhibits a small drift, limited in the range of 10 cm, which could be due to uncertainty in the position of the center of mass, terrain irregularities, and GPS resolution.

Although ideally the center of mass during a pivot turn remains fixed, the elasticity of the suspension probably causes the slight oscillation on the linear velocity components, in this case however the simulation results seem quite consistent with the measurements.

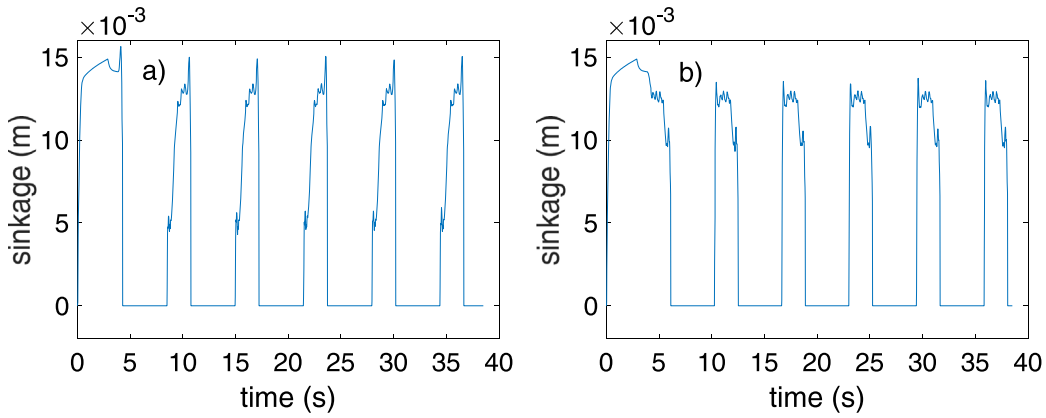

Fig. 19. Sinkages of the grouser of the 13th element of the left (a) and right (b) track.

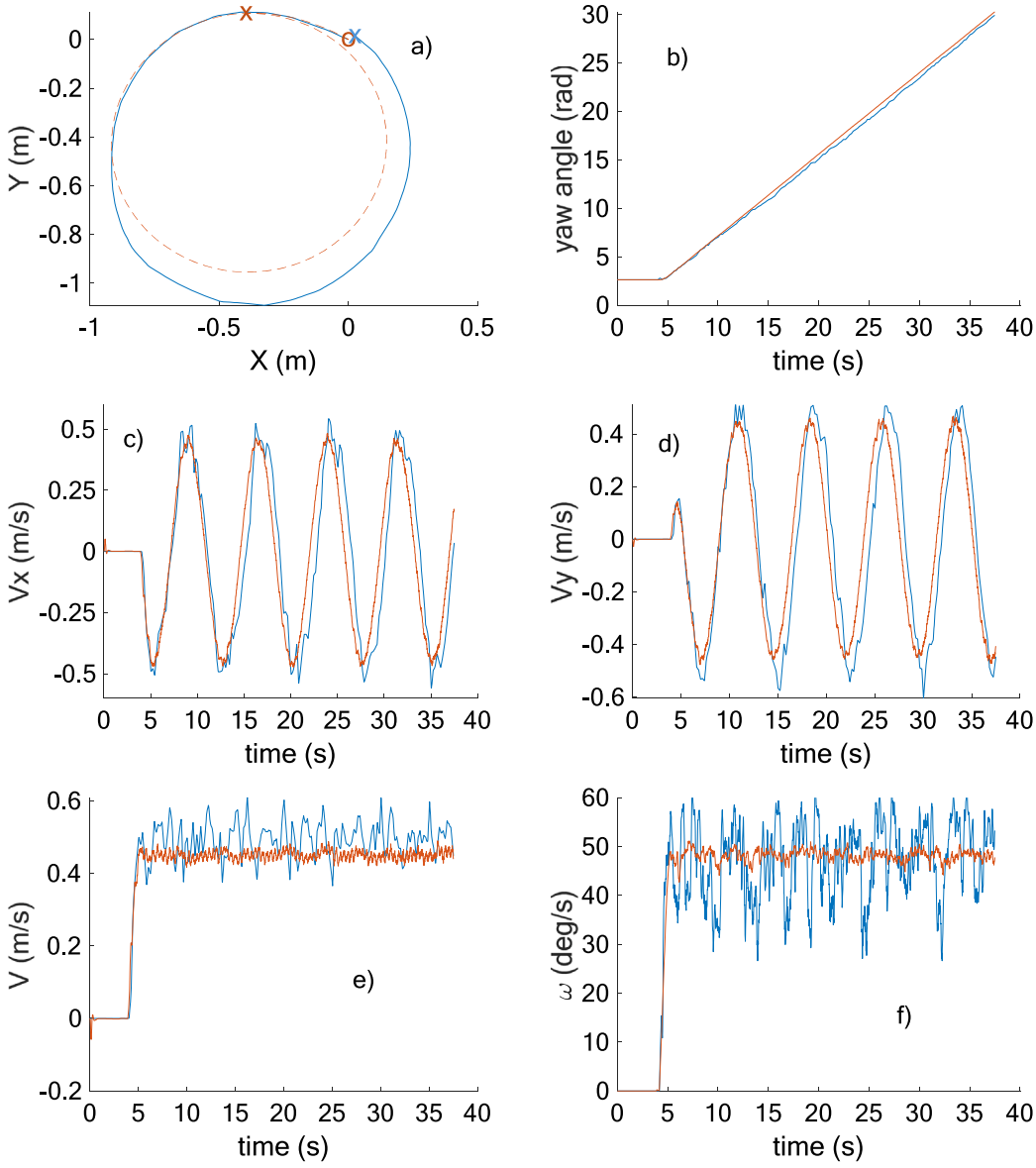

Fig. 20. Step steering: comparisons between simulations (red line) and experiments (blue line). (a) Trajectories of the center of mass in the horizontal plane; (b) yaw angle, TIC = 0.012; (c) velocity of the center of mass along the x axis, TIC = 0.216; (d) velocity of the center of mass along the y axis, TIC = 0.212; (e) linear velocity, TIC = 0.068; (f) angular velocity, TIC = 0.080.

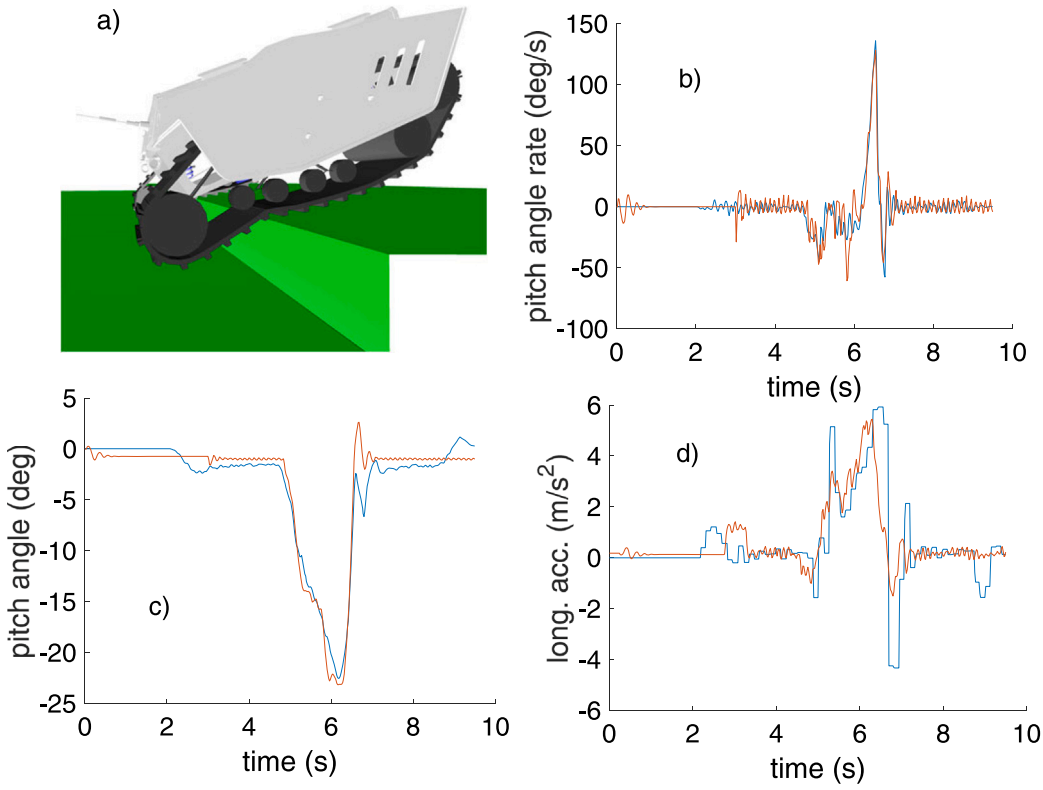

Fig. 21. Overcoming a step: comparisons between simulations (red line) and experiments (blue line). (a) Screenshot of the 3D animation generated by Dymola; (b) pitch angle rate, TIC = 0.229; (c) pitch angle, TIC = 0.101; (d) longitudinal acceleration, TIC = 0.374.

Of course, in this case the sinkage of grousers plays on important role, Fig. 19 shows the sinkages of the grouser of the 13th element of the right and left track.

3.2.2. Step steering

In a second experiment an angular velocity ω equal to 1 rad/s and a linear velocity V equal to 0.5 m/s were considered. Results are reported in Fig. 20.

3.3. Overcoming a step

In a last experiment the robot is commanded to move over a step of height 0.153 m with a linear velocity $V = 0.5$ m/s on a concrete (rigid) surface, characterized by a shear deformation modulus $K = 0.02$ mm and a friction coefficient $\mu_s = 0.9$.

In this case only IMU measurements have been considered.

Fig. 21.a shows a screenshot of the 3D animation generated by Dymola, Fig. 21.b shows the comparison between the measured and simulated pitch angle rate, while Fig. 21.c and d are relevant to the pitch angle and the longitudinal acceleration (all quantities are expressed in the IMU reference frame). Again, a good agreement is obtained.

4. Conclusion

This paper describes in detail the dynamic model of a tracked vehicle for agricultural applications.

This model, consisting of about 300,000 equations, is characterized by a high accuracy, both in the description of the mechanical structure, in particular of the suspensions, and, especially, in the description of the interaction with ground, which can be assumed to be either rigid or deformable. This accuracy was achieved thanks to the adoption of the object-oriented modelling language Modelica, which allowed a modular and hierarchical approach, distributing the complexity of the modelling on the individual components and leaving the interpreter, Dymola, the task of assembling the overall model. The result is a package that can also be processed by the open source interpreter OpenModelica, although for efficiency reasons in this article the commercial interpreter Dymola has been adopted.

Furthermore, the proposed model has been extensively experimentally validated, both in indoor (rigid terrain) and outdoor (deformable terrain) conditions, using a VICON motion capture system, consisting of 30 cameras and an IMU, in the indoor experiments, while a RTK GPS system was used in the outdoor experiments.

Besides its accuracy in reproducing vehicle dynamics and soil interaction, one of the most important strength of the proposed approach is that Modelica models can be exported, in the form of a Functional Mockup Unit (FMU) (Junghanns et al., 2021) to many different languages, e.g., Python, C++, and ROS (Macenski et al., 2022), to support different tasks, including simulation and optimization, or as a tool to develop Machine and Deep Learning applications.

For all the aforementioned reasons, the proposed model represents an important tool for the design and validation of motion planning and control strategies, and it is currently used for the design of slip estimation algorithms and of feedback linearizing controllers. Furthermore, the intrinsic modularity of object-oriented modelling languages allows the adoption of this model also as a tool for the optimization of the locomotion system of a tracked vehicle, or to assess the change to soil mechanical and hydraulic properties produced by different tracks in different soil conditions.

Finally, the main limitation of the approach is related to the computational complexity of the proposed model, that makes simulations a

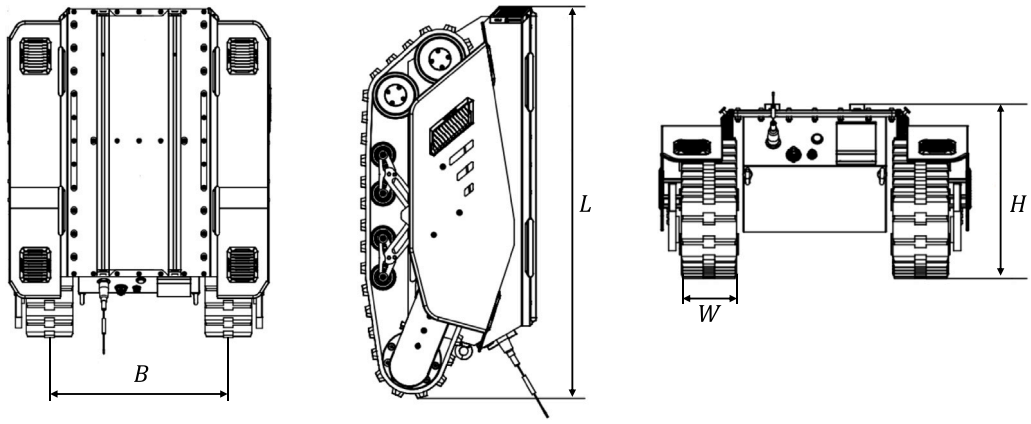

Fig. A.22. Geometric parameters.

computationally intensive task. Further developments will include the use of the model to train a Physics-Informed Neural Network, that will allow to reduce the simulation time.

CRediT authorship contribution statement

Alessandro Febbraro: Writing – review & editing, Writing – original draft, Visualization, Validation, Software, Methodology, Investigation, Data curation, Conceptualization. **Mattia Dutto:** Writing – review & editing, Visualization, Validation, Software, Data curation. **Luca Bascetta:** Writing – review & editing, Writing – original draft, Validation, Supervision, Software, Resources, Project administration, Investigation, Funding acquisition, Data curation, Conceptualization. **Gianni Ferretti:** Writing – review & editing, Writing – original draft, Validation, Supervision, Methodology, Investigation, Conceptualization.

Declaration of competing interest

The authors declare that they have no known competing financial interests or personal relationships that could have appeared to influence the work reported in this paper.

Acknowledgements

This study was conducted within the Agritech National Research Center and received funding from the European Union Next-GenerationEU (PIANO NAZIONALE DI RIPRESA E RESILIENZA (PNRR) – MISSIONE 4 COMPONENTE 2, INVESTIMENTO 1.4 – D.D. 1032 17/06/2022, CN00000022). One of the authors has received funding from the project PNRR-NGEU through the MUR – DM 118/2023. This manuscript reflects only the author's views and opinions, neither the European Union nor the European Commission can be considered responsible for them.

Appendix. Vehicle parameters

See Fig. A.22 and Table A.2.

Data availability

Models and validation data are available online at https://github.com/ROSETEA-lab/modelica_agilexbunker, a Modelica package has been created, containing the models of the validation experiments.

Table A.2
Vehicle parameters.

Parameter	Value	Unit
Number of wheels	8	–
Mass	180	kg
L	1064	mm
B	574	mm
H	473	mm
W	150	mm
Number of grousers	38	–
Stiffness of suspensions	131.39	N/mm

References

Andres, M., 2009. Object-Oriented Modeling of Wheels and Tires in Dymola/Modelica (Master's thesis). Vorarlberg University of Applied Sciences, Donbirn, Austria.

Bascetta, L., Ferretti, G., 2024. The role of autonomous ground vehicles in smart agriculture: Enabling control technologies for autonomous navigation. In: Reference Module in Materials Science and Materials Engineering. Elsevier.

Bechar, A., Vigneault, C., 2017. Agricultural robots for field operations. Part 2: Operations and systems. Biosyst. Eng. 153, 110–128.

Bekker, M., 1969. Introduction to Terrain-vehicle Systems. University of Michigan Press.

Bosso, N., Spiryagin, M., Gugliotta, A., Somà, A., 2013. Mechatronic Modeling of Real-Time Wheel-Rail Contact. Springer Berlin Heidelberg.

Botta, A., Cavallone, P., Baglieri, L., Colucci, G., Tagliavini, L., Quaglia, G., 2022. A review of robots, perception, and tasks in precision agriculture. Appl. Mech. 3 (3), 830–854.

Boudon, B., Dang, T.T., Margetts, R., Borutzky, W., Malburet, F., 2019. Simulation methods of rigid holonomic multibody systems with bond graphs. Adv. Mech. Eng. 11 (3), 1–29.

Dahlquist, E., Aparicio, E.T., Li, H., Fritzson, P., Östlund, P., 2013. Comparison OpenModelica - Dymola for power plant simulation. SNE Simul. Notes Eur. 23 (3–4).

Decostere, B., Craene, J., Hoey, S., Vervaeren, H., Nopens, I., Van Hulle, S., 2016. Validation of a microalgal growth model accounting with inorganic carbon and nutrient kinetics for wastewater treatment. Chem. Eng. J. 285, 189–197.

Dempsey, M., 2006. Dymola for multi-engineering modelling and simulation. In: IEEE Vehicle Power and Propulsion Conference. pp. 1–6.

Dorado-Rojas, S.A., Navarro Catalán, M., de Castro Fernandes, M., Vanfretti, L., 2020. Performance benchmark of Modelica time-domain power system automated simulations using Python. In: American Modelica Conference 2020, Boulder, Colorado, USA, March 23-25, 2020. Linköping University Electronic Press, pp. 28–35.

Droukas, L., Doulgeri, Z., Tsakiridis, N.L., Triantafyllou, D., Kleitsiotis, I., Mariolis, I., Giakoumis, D., Tzovaras, D., Kateris, D., Bochtis, D., 2023. A survey of robotic harvesting systems and enabling technologies. J. Intell. Robot. Syst. 107 (2), 1–29.

Elaoud, A., Chehaibi, S., 2011. Soil compaction due to tractor traffic. J. Fail. Anal. Prev. 11, 539–545.

Elmqvist, H., Mattsson, S.E., Olsson, H., 2014. Parallel model execution on many cores. In: 10th International Modelica Conference, March 10-12, 2014, Lund, Sweden. In: Modelica, Linköping University Electronic Press, pp. 363–370.

Fathallah, F.A., 2010. Musculoskeletal disorders in labor-intensive agriculture. Appl. Ergon. 41 (6), 738–743.

Ferretti, G., Girelli, R., 1999. Modelling and simulation of an agricultural tracked vehicle. J. Terramech. 36 (3), 139–158.

Fritzson, P., Pop, A., Abdelhak, K., Ashgar, A., Bachmann, B., Braun, W., Bouskela, D., Braun, R., Buffoni, L., Casella, F., Castro, R., Franke, R., Fritzson, D., Gebremedhin, M., Heuermann, A., Lie, B., Mengist, A., Mikelsons, L., Moudgalya, K., Ochel, L., Palanisamy, A., Ruge, V., Schamai, W., Sjölund, M., Thiele, B., Tinnerholm, J., Östlund, P., 2020. The OpenModelica integrated environment for modeling, simulation, and model-based development. Model. Identif. Control 41 (4), 241–295.

Gebbers, R., Adamchuk, V.I., 2010. Precision agriculture and food security. Science 327 (5967), 828–831.

Goel, R.K., Yadav, C.S., Vishnoi, S., Rastogi, R., 2021. Smart agriculture – Urgent need of the day in developing countries. Sustain. Comput.: Inform. Syst. 30, 100512.

Grazioso, A., di Maria, E., Giannoccaro, N.I., Ishii, K., 2022a. Multibody modeling of a new wheel/track reconfigurable locomotion system for a small farming vehicle. Mach. 10 (12), 1117.

Grazioso, A., Galati, R., Mantriota, G., Reina, G., 2022b. Advances in Italian mechanism science. In: Ch. Multibody Simulation of a Novel Tracked Robot with Innovative Passive Suspension. Springer International Publishing, pp. 139–146.

Grazioso, A., Ugenti, A., Galati, R., Mantriota, G., Reina, G., 2023. Modeling and validation of a novel tracked robot via multibody dynamics. Robotica 41 (10), 3211–3232.

Harnisch, C., Lach, B., Jakobs, R., Troulis, M., Nehls, O., 2005. A new tyre-soil interaction model for vehicle simulation on deformable ground. Veh. Syst. Dyn. 43, 384–394.

Janosi, Z.J., Hanamoto, B., 1961. The analytical determination of drawbar pull as a function of slip for tracked vehicles in deformable soils. In: 1st International Conference of the International Society for Terrain-Vehicle Systems. Turin.

Junghanns, A., Gomes, C., Schulze, C., Schuch, K., Mai, P., Blaesken, M., Zacharias, I., Pillekeit, A., Wernersson, K., Sommer, T., Bertsch, C., Blochwitz, T., Najafi, M., 2021. The functional mock-up interface 3.0 - New features enabling new applications. In: 14th Modelica Conference 2021, Linköping, Sweden. pp. 17–26.

Kutzbach, H.D., 2000. Trends in power and machinery. J. Agric. Eng. Res. 76 (3), 237–247.

Liu, Y., Ma, X., Shu, L., Hancke, G.P., Abu-Mahfouz, A.M., 2021. From industry 4.0 to agriculture 4.0: Current status, enabling technologies, and research challenges. IEEE Trans. Ind. Inform. 17 (6), 4322–4334.

Macenski, S., Foote, T., Gerkey, B., Lalancette, C., Woodall, W., 2022. Robot operating system 2: Design, architecture, and uses in the wild. Science Robotics 7 (66), eabm6074.

Maffezzoni, C., Girelli, R., 1998. MOSES: modular modelling of physical systems in an object-oriented database. Math. Comput. Model. Dyn. Syst. 4 (2), 121–147.

Marinoudi, V., Sørensen, C.G., Pearson, S., Bochtis, D., 2019. Robotics and labour in agriculture. A context consideration. Biosyst. Eng. 184, 111–121.

Mattsson, S.E., Elmqvist, H., Otter, M., 1998. Physical system modeling with Modelica. Control Eng. Pract. 6 (4), 501–510.

Miller, S., 2024. Tracked vehicle model with simscape. Github.com/simscape/Tracked-Vehicles-Simscape.

Mocera, F., Nicolini, A., 2018. Multibody simulation of a small size farming tracked vehicle. Procedia Struct. Integr. 8, 118–125.

Mocera, F., Soma, A., 2017. Study of a Hardware-In-the-Loop bench for hybrid electric working vehicles simulation. In: 12th International Conference on Ecological Vehicles and Renewable Energies. IEEE, pp. 1–8.

Mocera, F., Somà, A., Nicolini, A., 2020. Grousers effect in tracked vehicle multibody dynamics with deformable terrain contact model. Appl. Sci. 10 (18), 6581.

Nicolini, A., Mocera, F., Soma, A., 2018. Multibody simulation of a tracked vehicle with deformable ground contact model. Proc. Inst. Mech. Eng. K 233, 146441931878429.

Oestersötebier, F., Wang, P., Trächtler, A., 2014. A modelica contact library for idealized simulation of independently defined contact surfaces. In: 10th International Modelica Conference. Lund, Sweden, pp. 929–937.

Özdemir, M.N., 2016. Steering Dynamics of Tracked Vehicles (Master's thesis). Middle East Technical University.

Özdemir, M., Kilic, V., Unlusoy, Y.S., 2016. Transient tracked vehicle steering model. In: ISTVS 8th Americas Regional Conference. pp. 1–19.

Özdemir, M.N., Kılıç, V., Ünlüsoy, Y.S., 2017. A new contact and slip model for tracked vehicle transient dynamics on hard ground. J. Terramech. 73, 3–23.

Pierce, F.J., Nowak, P., 1999. Advances in agronomy volume 67. In: Ch. Aspects of Precision Agriculture. Elsevier, pp. 1–85.

Proto, A.R., Zimbalatti, G., 2010. Risk assessment of repetitive movements in the citrus fruit industry. J. Agric. Saf. Health 16 (4), 219–228.

Qin, Y., Cheng, B., Deng, X., 2014. Trajectory optimization of flapping wings modeled as a three degree-of-freedoms oscillation system. In: IEEE/RSJ International Conference on Intelligent Robots and Systems. pp. 3193–3200.

Said Mohamed, E., Belal, A., Kotb Abd-Elmabod, S., El-Shirbeny, M.A., Gad, A., Zahran, M.B., 2021. Smart farming for improving agricultural management. Egypt. J. Remote Sens. Space Sci. 24 (3), 971–981.

Slaughter, D., Giles, D., Downey, D., 2008. Autonomous robotic weed control systems: A review. Comput. Electron. Agric. 61 (1), 63–78.

Subeesh, A., Mehta, C., 2021. Automation and digitization of agriculture using artificial intelligence and internet of things. Artif. Intell. Agric. 5, 278–291.

Tiozzo Fasiolo, D., Scalera, L., Maset, E., Gasparetto, A., 2023. Towards autonomous mapping in agriculture: A review of supportive technologies for ground robotics. Robot. Auton. Syst. 169, 104514.

Wong, J.Y., 2001. Theory of Ground Vehicles, third ed. Wiley.

Yépez-Ponce, D.F., Salcedo, J.V., Rosero-Montalvo, P.D., Sanchis, J., 2023. Mobile robotics in smart farming: current trends and applications. Front. Artif. Intell. 6, 1–13.

Zhang, Q., Karkee, M., Tabb, A., 2019a. Burleigh dodds series in agricultural science. In: Ch. the Use of Agricultural Robots in Orchard Management. Burleigh Dodds Science Publishing, pp. 187–214.

Zhang, Z., Wang, Y., Zhang, Z., Li, D., Wu, Z., Bai, R., Meng, G., 2019b. Ergonomic and efficiency analysis of conventional apple harvest process. Int J. Agric. Biol. Eng. 12 (2), 210–217.

Zhang, Z., Zhang, Z., Wang, X., Liu, H., Wang, Y., Wang, W., 2019c. Models for economic evaluation of multi-purpose apple harvest platform and software development. Int. J. Agric. Biol. Eng. 12 (1), 74–83.